Nanofabrication of Hybrid Optoelectronic Devices

Nanofabrication of Hybrid Optoelectronic Devices

A dissertation presented

by

Alan Michael Dibos

to

The School of Engineering and Applied Sciences

In partial fulfillment of the requirements
for the degree of

Doctor of Philosophy

in the subject of

Applied Physics

Harvard University

Cambridge, Massachusetts

January 2015

Thesis Advisor

Professor Hongkun Park

Author

Alan Michael Dibos

Nanofabrication of Hybrid Optoelectronic Devices

Abstract

The material requirements for optoelectronic devices can vary dramatically depending on the application. Often disparate material systems need to be combined to allow for full device functionality. At the nanometer scale, this can often be challenging because of the inherent chemical and structural incompatibilities of nanofabrication. This dissertation concerns the integration of seemingly dissimilar materials into hybrid optoelectronic devices for photovoltaic, plasmonic, and photonic applications. First, we show that combining a single strip of conjugated polymer and inorganic nanowire can yield a nanoscale solar cell, and modeling of optical absorption and exciton diffusion in this device can provide insight into the efficiency of charge separation. Second, we use an on-chip nanowire light emitting diode to pump a colloidal quantum dot coupled to a silver waveguide. The resulting device is an electro-optic single plasmon source. Finally,

we transfer diamond waveguides onto near-field avalanche photodiodes fabricated from GaAs. Embedded in the diamond waveguides are nitrogen vacancy color centers, and the mapping of emission from these single-photon sources is demonstrated using our on-chip detectors, eliminating the need for external photodetectors on an optical table. These studies show the promise of hybrid optoelectronic devices at the nanoscale with applications in alternative energy, optical communication, and quantum optics.

Contents

List of Figures

Acknowledgements

Pursuing a PhD has been an immensely challenging and trying experience, and I am extremely grateful for the professional and personal relationships I have drawn on over the years for support. In my experience, scientific research (particularly the nanofabrication necessary to get to the science) is a rollercoaster of elation and heartbreak. Devices appear to work, turn out not to, and require you to grind out technical problems to obtain results. I could not have persevered through the trials of graduate school without the help of many people.

First, I must thank my advisor, Prof. Hongkun Park, who has put up with me for many years. He has a keen eye for determining which scientific problems are worth investigating, and within a few minutes he can immediately evaluate why many experiments fail. I hope that I have picked up his knack for this under his tutelage. In addition, he is never afraid of exploring a new topic because no one in his group has the appropriate expertise. I've gained so much experience by working on disparate projects

with him (several not covered in this dissertation), and I believe it's unlikely many other advisors would be so willing to support a graduate student on projects and methods that are so far outside the group's comfort zone.

Prof. Misha Lukin has been extremely generous with his laboratory resources, and I would not have been able to carry out the diamond-on-GaAs experiments without some of the equipment and personnel in his group. Similarly, I would like to thank Prof. Anna Fontcuberta i Morral and her students, who provided me with the first GaAs nanowires early on in my PhD. Even though the project evolved away from those nanowires, it started the avalanche (pun intended) of work that evolved into my final project. I need to express my appreciation to Prof. Charles Lieber and his students for providing our group with the core-shell nanowires we used for generating the single plasmon source. I would also like to thank my committee members, Prof. Marko Loncar and Prof. Philip Kim, for taking the time to provide me with feedback about my work.

I would like to thank a number of the scientists who trained me when I first started my PhD. In particular, Kristin Maher and Dong Yu were instrumental in showing me the ropes as a G1-2. They got me started on the initial P3HT experiments that I took over and evolved into the study in Chapter 2. I learned a lot from Abram Falk and Frank Koppens regarding how to think carefully about measurements.

I had the pleasure of working with Chun Yu and Mingzhao Liu on a variety of projects for many years. Chun was the most pleasant colleague who always had a smile on his face and a joke to tell. Mingzhao was the driving force behind the InGaN LED project, and he seemed to have more knowledge crammed into his head than anyone I've

ever met. He really inspired me to always try to learn about different topics because you never know what will be useful in the future.

I had pleasure of working with Jacob Robinson for several years. To this day he is a great friend who always seems to be able to bounce back and forth between serious discussions about science and college basketball. Similarly, I would like to thank Alex High for being such a good friend and supportive colleague. These last couple of years would have been especially tough if you weren't around for discussions over an IPA. Likewise, I would like to express thanks to Marsela Jorgolli and Mark Polking who were always available for discussion, serious and otherwise over the years. To any other members of the Park group I didn't mention, I appreciate all the support.

I'm highly indebted to a number of people from the Lukin group who patiently advised me about confocal microscopy and helped me with diamond samples. Ruffin Evans, Kristiaan de Greve, and Brendan Shields were especially instrumental in being able to complete these experiments.

There are so many staff members at Harvard who have helped me over the years. In particular the CNS staff—JD Deng, Yuan Lu, Steve Paolini, and Dave LaFleur—have gone above and beyond to help me to complete these huge fabrication projects and bailed me out when equipment went down. Steve Sansone in the machine shop helped immeasurably when I was building our new confocal microscope.

By far my most influential colleague over the years has been Nathalie de Leon. She has served as a scientific big sister to me, and helped me with all aspects of my scientific career. Thank you so much for the countless discussions, collaborations, and always being willing to go eat Indian food for lunch.

Finally, there is no one I need to thank more than my wonderful fiancé, Abra. She has been so patient with the late nights doing fabrication and missed vacations trying to finish up my PhD. Absolutely none of this would have been possible without her.

Dedicated to my parents for always believing in me.

Chapter 1

Properties of Hybrid Nanostructures

1.1 Overview

Synergy is commonly defined as the whole being greater than the sum of its parts. This has countless examples in nature, including the well-known symbiotic relationships between bees and pollinating flowers as well as bacteria residing in the human intestines. Synergy can be an equally powerful force in the development of technology, including optical devices. All material systems have limitations, but combining two or more materials with complimentary properties can lead the way toward novel and better performing devices. In this thesis we will present three projects that all directly involve

the combination of complimentary optical materials into so called "hybrid" nanostructures.

Environmentally friendly renewable sources of energy have been a burgeoning scientific and public policy topic over the past several decades. Among the many renewable energy alternatives to fossil fuels are solar-based sources, including photovoltaic and solar thermal technologies. Bulk heterojunction photovoltaic solar cells—most often a mixture of electron donor conductive polymers and electron acceptor inorganic nanostructures—may be a complimentary technology to conventional semiconductor solar cells for particular applications. This is due to their solution processable components and low process temperatures, which may be suitable for fabrication onto lightweight, flexible substrates. Power conversion efficiencies are still well below that of commercial silicon-based technologies, but single layer devices have improved substantially over the past two decades to near 8%[1,2] with tandem cells above 10%.[1] Quantification of the loss mechanisms under different operating conditions is essential to further improve device performance. Beyond the potential technological, economic, and societal benefits of such research, there is an opportunity to explore the rich physics of exciton generation, transport, and dissociation that differs greatly from conventional semiconductor devices. Chapter 1.2 provides a brief introduction to these excitonic processes.

Chapter 2 discusses experiments to investigate a model version of a bulk heterojunction solar cell. This model solar cell is a hybrid device consisting of a single heterojunction between a strip of conjugated polymer and an inorganic semiconductor nanowire (NW). This simplified geometry allows for reliable accounting of light

absorption in the different material components and hence their respective exciton generation rates. Using this method, it is possible to distinguish between various loss mechanisms and set an upper bound on the device efficiency if scaled up to a fully functioning bulk heterojunction solar cell.

Nanoscale optical circuits employing single photons are another exciting area of scientific inquiry. Single photons are excellent carriers of quantum information because they can propagate long distances without loss of coherence,[3,4] making them useful in quantum encryption and quantum computation. In addition to these quantum applications, if the single photons are reliably generated and collected with unity efficiency, one can use them for ultra-low power optical communication.

The simplest integrated single photon circuit consists of 3 components: (1) an on-chip source, (2) an on-chip detector, and (3) a transmission pathway to route photons between the two. However, efficient, on-demand generation and collection of single photons is an outstanding technological problem. Typically, single photons are generated by parametric down-conversion, in which the creation of a single photon is heralded.[5,6] Another approach is to employ solid-state quantum emitters as the source of single photons, such as semiconductor quantum dots and atom-like defects in wide bandgap semiconductors. The solid-state nature of these emitters provides the exciting opportunity to use semiconductor fabrication techniques to build integrated sources and detectors for on-chip optical circuits. However, these "artificial atoms" are generally sensitive to their external environment thereby limiting the fabrication processes that can be used. An added complication is that epitaxial quantum dots and color centers in wide bandgap semiconductors, such as the nitrogen vacancy (NV) center in diamond, are typically

embedded in a high refractive index host material, which makes it extremely difficult to collect a high percentage of emitted photons via a far-field detection scheme (see Chapter 1.4). Thus the push for integrated photonic circuits isn't just a quest for miniaturization for its own sake, rather near-field pumping and collection schemes hold promise for much greater device efficiency.

Integrated optical circuit elements at size scales near or above the diffraction limit, almost universally rely on photonic waveguides to route photons via total internal reflection. These waveguides allow for extremely low loss transmission of photons. There is a large body of literature about the fabrication of photonic waveguides as well as more complicated structures such as ring resonators and photonic crystal cavities to allow for manipulation of the guided photons.

A promising method to further miniaturize an optical circuit below the diffraction limit is to employ surface plasmon polaritons (SPPs), which are propagating optoelectronic excitations along a metal-dielectric interface (see Chapter 1.3). Light in the form of an SPP can spatially concentrate light far below the diffraction limit at the expense of increased propagation loss compared to a photonic mode in a dielectric waveguide. Furthermore, a quantum emitter placed in the vicinity of a plasmonic waveguide such as silver, can collect a large fraction of the photons emitted and then have them propagate as SPPs along the waveguide.

Chapters 3 and 4 of this thesis discuss two experiments that each use a hybrid structure of a semiconductor diode (source or detector) joined to a waveguide that is coupled strongly to a quantum emitter. Each experiment represents two-thirds of the simple integrated single photon circuit mentioned above. More specifically, Chapter 3

presents a proof-of-principle demonstration of pumping a colloidal semiconductor quantum dot with an on-chip LED, and subsequent collection of the single photons as SPPs by a silver nanowire plasmonic waveguide. Chapter 4 discusses a project whereby a nitrogen vacancy center embedded in a diamond photonic waveguide is pumped by an external laser, and the fluorescence is detected via a near-field gallium arsenside (GaAs) avalanche photodiode.

Overall the three projects presented in this thesis have distinct goals, but all three rely heavily on the nanofabrication of hybrid optoelectronic elements. It is through the use of these complimentary optical materials that progress can be made toward novel devices with applications in renewable energy, optical communication, and quantum optics.

1.2 Exciton Generation, Diffusion, and Separation in Conjugated Polymers

The general process of turning an absorbed photon in a conjugated polymer into photocurrent has been readily discussed in the literature[7,8] and is shown in Figure 1.1. This process first involves the absorption of a photon in the polymer to create an exciton with a binding energy much larger than the thermal energy under standard operating conditions. The exciton can diffuse to the donor/acceptor interface (the exciton diffusion length is typically ≤ 10 nm). The exciton dissociates at the junction and create an electron-hole pair bound at the interface by Coulombic attraction. Finally, the bound pair separates and the free carriers are transported via drift/diffusion as majority carriers to the electrodes. An exciton that doesn't reach the interface before relaxation cannot contribute to the photocurrent. The materials in these solar cells are complimentary: the polymer

contributes greatly to photon absorption and hole conduction, whereas the inorganic component contributes to photon absorption, assists the charge transfer, and provides an electron conduction pathway. The short exciton diffusion length in the polymer necessitates the nanoscale morphology of these components.

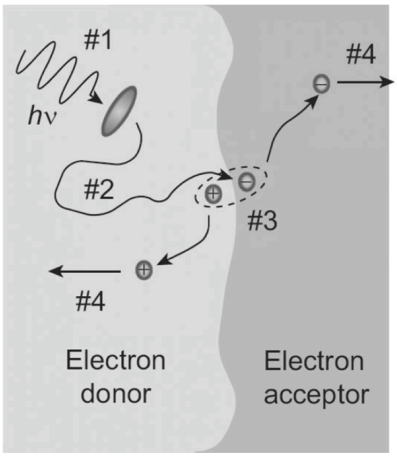

Figure 1.1 | Exciton generation, diffusion, and dissociation in hybrid photovoltaic devices. A photon excites the electron donor phase creating an exciton with binding energy of ~0.4 eV, shown in step #1. The exciton then diffuses (step #2) to a donor/acceptor interface where it dissociates into a bound electron–hole pair. Excitons that do not reach an interface recombine and do not contribute to photocurrent. Step #3 represents the separation of electron–hole pairs bound at the interface by their mutual Coulomb attraction. The efficiency of this process depends on temperature, electric field, and the initial pair separation. Step #4 then represents the bulk transport of free charges to the electrodes for collection. Figure and caption adapted from Ref. 7.

In spite of the large body of literature on bulk heterojunction solar cells, the details of the exciton diffusion and charge separation processes are still under investigation. The exciton diffusion length in a well-studied conjugated polymer such as P3HT has been reported with values varying from 2.5 to 10 nm.[9,10] In addition, the all-important charge separation process is still poorly understood. There are reports that temperature, electric field,[11] recombination,[12] and space charge[13] can limit the charge separation efficiency.

Other studies have suggested that the charge separation is a near unity efficiency process.[14]

Unfortunately, the vast majority of bulk heterojunction devices have many additional potential loss channels such as electrical shorts between electrodes (unless there are separate electron and hole blocking layers), incomplete hopping networks for charge transport, and recombination.[12,15] These additional loss mechanisms make it difficult to quantify the charge separation efficiency using a fully assembled device. In Chapter 2, we present a well-controlled model system to further investigate the charge separation process.

1.3 Plasmonic waveguides coupling to quantum emitters

A surface plasmon polariton (SPP) is an electromagnetic wave that propagates along a metal-dielectric interface. It consists of the coupling of the electromagnetic fields with the induced charge oscillations in the metal. Compared with a free space photon at the same frequency, an SPP has more momentum, higher optical confinement, and a lower propagation velocity.

Solving Maxwell's equations at a simple planar interface between a metal and a dielectric produces a confined optical mode with wave vector k_{SPP} given by:

$$k_{SPP}(\omega) = k_0 \sqrt{\frac{\varepsilon_d(\omega) \cdot \varepsilon_m(\omega)}{\varepsilon_d(\omega) + \varepsilon_m(\omega)}}$$

where k_0 is the wave vector of the free-space photon, and ε_m and ε_d are the frequency-dependent dielectric constants of the metal and dielectric, respectively. It is important to point out that these SPPs have a non-zero real component of their wave vector, so they

propagate in a given direction and can be waveguided similarly to photons. However, unlike photons in free space, there is a non-zero imaginary part of k_{SPP}, which represents propagation losses, in which the finite conductivity of the metal causes dissipative losses as the SPP propagates. Many metals and semiconductors can support SPP propagation, but for visible wavelengths the lowest propagation losses are associated with silver.

SPP waveguides, like their dielectric counterparts, are spectrally broadband. The main advantage of SPP waveguides over dielectric ones is that they can support modes with very small wavelengths, enabling highly sub-wavelength optical confinement. As the width of a dielectric waveguide shrinks below the optical wavelength, the electromagnetic fields will be squeezed out of the waveguide and eventually cease to be guided. On the other hand, plasmon waveguides can guide SPPs even when the waveguide dimensions are substantially narrower than the free space wavelength.

In addition to the planar SPP mode discussed above, guided SPP modes have been demonstrated in a number of geometries including metal wires surrounded by a dielectric,[16] metal-insulator-metal slab waveguides,[17] metallic grooves,[18] hybrid gap structures of high refractive index dielectric/low refractive index dielectric/metal,[19,20] and even chains of metal dots.[21] Because of the momentum mismatch between the plasmonic modes and free-space, SPPs should not—in principle—be easily converted to into free-space photons. In practice, because the SPP wavelength is smaller than the corresponding free-space wavelength, small defects along the surface of the metal such as grain boundaries can cause significant scattering. Chemically synthesized Ag nanowires (NWs) exhibit fewer defects than lithographically defined strips of evaporated Ag. They are

highly crystalline and have a smooth surface, and they allow SPPs to propagate for a long distance without being scattered, except at the ends of the nanowire.

Even with defect-free SPP waveguides, the propagation losses are sufficiently high to make them of limited usefulness for applications strictly involving long distance propagation, especially when compared with low-loss photonic waveguides. The beauty of plasmonic structures lies in fact that high optical confinement of SPPs also leads to a strong interaction with nearby optical emitters. SPP waveguides can function as antennas, capturing a high percentage of a nanoscale light source's emission. Moreover, the Purcell effect can cause the rate of spontaneous emission of a nanoscale emitter within the near field of an SPP waveguide to be modified. The total radiation rate of an emitter can be broken down into its component radiation rates $\Gamma_{\text{total}} = \Gamma_{\text{cavity}} + \Gamma_{\text{free-space}} + \Gamma_{\text{non-radiative}}$, and the definition of the Purcell factor (P) is given by, $P = \Gamma_{total} / \Gamma_0$ where Γ_0 is the emission rate if the emitter were in vacuum. It has been shown that the optimized Purcell factor of an emitter near a metal nanowire scales as $P \propto 1/(k_0 R)^3$, where R is the radius of the nanowire.[22] Therefore, a SPP waveguide that is significantly thinner than the free-space wavelength can have a high Purcell factor *even when there is no longitudinal confinement along the nanowire axis*. Photonic crystals with high quality factors can be used to generate large Purcell enhancements,[23] but even a simple 1D plasmon waveguide can generate a significant degree of emission modification. Furthermore, when an optical resonator is constructed around a plasmonic waveguide, extremely large Purcell enhancements can be observed, in spite of the low cavity quality factor.[24] This can be particularly useful because the relatively broad linewidth of a plasmonic cavity resonance

doesn't need to be tuned as precisely as a high Q cavity to achieve the same level of Purcell enhancement.

Plasmonics can be useful, in particular, for coupling to *single* photon sources as well. Single photons can also be generated by optically pumping a quantum emitter such as colloidal quantum dot (QD), which has discrete electronic states due to quantum confinement, allowing it to emit single photons at its first exciton energy.[25] A previous demonstration showed that single SPPs could be generated from pumping colloidal quantum dots coupled to Ag NW waveguides.[26] By optimizing the spacing between CdSe QDs and 100 nm diameter Ag NWs with a polymer spacer, Akimov *et al.* showed that the emission from a single QD could be directed primarily into SPPs, with a coupling efficiency up to 60% and a Purcell factor of ~2. They also showed that the photon cross-correlation function of SPPs scattered at the end of the nanowire and photons emitted into free space from the QD shows clear anti-bunching, proving that the quantum dot functions as a single plasmon source. This experiment proved that a simple 1D SPP waveguide could serve as an efficient means for collecting single photons.

This initial demonstration relied on far-field excitation of the quantum dot, which requires a bulky external laser. Conversely, single photons can be generated electrically on-chip by embedding self-assembled quantum dots into the intrinsic region of a *p-i-n* light emitting diode (LED), as has been previously shown in the InAs/GaAs system.[27,28] However, since the quantum emitters are buried deep within a high refractive index material, they are not accessible from the near field, and the far field photon collection efficiency is as low as a few percent.[29]

We will exploit a few of these features of plasmon waveguides in Chapter 3. We explore a hybrid approach of building an on-chip LED to pump a single CdSe QD coupled to a Ag NW plasmon waveguide, thereby creating an electro-optic single plasmon source.

1.4 Nitrogen Vacancy Centers in Waveguides Fabricated from Bulk Diamond

Color centers in wide band gap semiconductors are a promising materials platform, both for fundamental experiments in quantum optics and atomic physics because these are lattice-substitutional defects with electronic states that are located deep within the band gap. Thus these defects behave as atomic-like systems in the solid state. While there are many colors centers being investigated today in silicon carbide,[30] zinc oxide,[31] and diamond,[32] the negatively charged nitrogen-vacancy (NV) defect in diamond is the most well-known example.

The negatively charged NV center is a nitrogen ion substituted into the diamond lattice next to a vacancy (missing carbon atom). This remarkable defect center is a stable source of single photons at room temperature.[33] The fluorescence has two components, the zero phonon line (ZPL) with "atom-like" emission, which is at 637 nm, and the phonon sidebands from thermal broadening, which are from ~600 nm to the NIR.[33,34] Due to its energy level structure, NV fluorescence is spin-state dependent, allowing simple routes for optical initialization and readout. Even at room-temperature the spin coherence times are long allowing for many potential operations on a single spin.[35]

One can broadly define two different sets of applications involving an NV center, those that require cryogenic temperatures and those that do not. Room temperature measurements of NV centers in diamond have many potential applications including fluorescence markers in biological cells,[36] nanoscale thermometry,[37] nanoscale magnetic[38] and electric-field sensing,[39] and nanoscale spin detection.[40] If cooled down to liquid helium temperature, the NV^- can be used as an optically addressable solid-state spin-qubit, and can be employed in quantum networks and quantum registers.[41]

There are two primary motivating factors for wanting to perform optical readout of a quantum emitter via near-field detectors. The most obvious reason is that near-field detection allows for photon collection without the need for bulky external photodetectors (often on an optical table) for more compact and scalable devices. The second reason is that diamond has a fairly large refractive index (n=2.4) and many photons emitted by a color center cannot be collected efficiently using external optics because they are trapped in the diamond via total internal reflection.[42]

There have been many experiments demonstrating improved collection efficiency from bulk diamond without pursuing near-field photodetection. One solution to this problem is to engineer a solid immersion lens (SIL)[43,44] or vertical nanowires[42] into the diamond substrate surface to increase the count rate. For example by transferring bulk diamond onto a transparent material with higher refractive index, many more photons can be collected.[45,46] This is difficult to do with bulk diamond because the refractive index is high, but can be accomplished by using a material such as gallium phosphide (n=3.3) and adding a SIL on the backside of the GaP to direct emission to a separate microscope objective lens.[47] This demonstration is impressive but the emission pattern coming from

the GaP SIL has mode poor overlap with a single-mode fiber typically used for collection in confocal microscopy, thereby greatly increasing background count rates. A simpler scheme can be employed if the diamond is first made into a nanostructure that has a greatly reduced effective refractive index, and then is transferred onto a glass cover slip. When fluorescence is collected via a standard oil immersion lens in this geometry, photon count rates very close to 1 Mcps can be achieved.[48]

These demonstrations of improved photon collection efficiency in bulk diamond are notable, but the best long-term solution is to develop optical networks on chip that involve waveguides, sources, detectors, resonators, modulators, etc. as has been achieved in other material systems. The light confinement for many of these nanophotonic structures is provided by total internal reflection, which requires refractive index contrast between the device and the surrounding medium. This is generally possible through the use of material heterostructures such as GaAs/AlGaAs/GaAs or silicon-on-insulator. The material of interest can be suspended in air because the sacrificial layer underneath can be etched away (or the sacrificial layer has a sufficiently low refractive index to still allow for guided modes in the top layer). Single-crystal diamond is difficult to grow on other materials because of its small lattice constant, making an epitaxial sacrificial layer geometry thus far unattainable.

However, there have been recent developments on the micro- and nanomachining of bulk diamond films. Focused ion beam (FIB) milling[49] has been used to realize nanoscale mechanical or optical structures in single-crystal diamond, but the diamond is generally damaged due to fabrication-induced imperfections, such as Ga implantation, which often limits device performance.

One creative but labor-intensive alternative to epitaxy involves the thinning of bulk diamond substrates into thin membranes on a Si handle wafer.[50] Lithography and reactive ion etching (RIE) are used to fabricate rectangular cross-section waveguides and cavities, and partial wet etching of the Si handle layer suspends the structures. The biggest issue with this technique is that the wedge angle of the diamond from polishing limits the area of the diamond chip with the desired device thickness.

A more scalable approach has been developed using a two-step reactive ion etching process in monolithic diamond to circumvent these problems.[51] As shown in Figure 1.2, the nanofabrication process is used to generate a triangular cross-section waveguide. The first step is to pattern a hard mask onto bulk diamond using photo- or electron-beam lithography. Then a top-down reactive ion etch is performed in an oxygen plasma. The sample is placed in an angled Faraday cage, and a second oxygen etch is performed. The Faraday cage consists of a metallic mesh with small openings on the surface, and it mimics a perfect hollow conductor and creates an effectively electric-field-free zone inside. This means the electric potential gradient of the plasma builds up over the face of the Faraday cage and accelerates ions along a path normal to the cage surface. Once the ions move past the metal grid and inside the cage, they travel ballistically toward the sample and undercut it to produce a suspended diamond nanobeam. This technique has been further developed to generate photonic crystal cavities and ring resonators with high quality factors in both implanted[52] and CVD-grown diamond.[53]

These suspended diamond waveguides can serve as a building block for nanophotonic circuits involving NV centers. At this point, it would be most advantageous to employ a near-field photon detector that naturally incorporates the waveguides. This could provide

all the benefits of very high photon collection efficiency from SILs or placing nanostructured NVs on glass cover slips, but without the need for external collection optics and detectors.

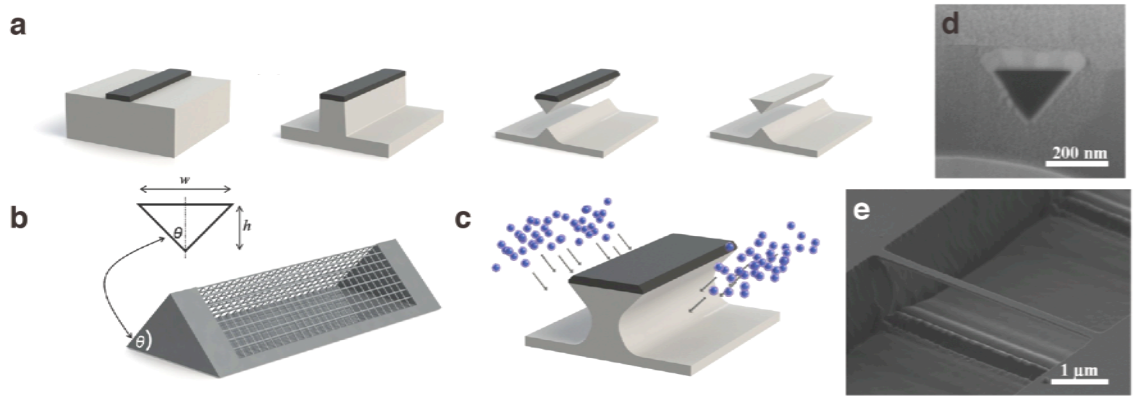

Figure 1.2 | Fabrication of free-standing diamond beams using a Faraday Cage. (a) Angled-etching fabrication schematic. **(b)** Schematic of triangular prism Faraday cage design with inset showing the relationship between the prescribed etch angle and the nanobeam bottom apex. **(c)** Illustration of angled-etching from two directions accomplished with the triangular prism Faraday cage design. **(d)** SEM images of FIB cross-sectioned ~250 nm wide solid diamond nanobeam. **(e)** SEM image of 200 nm wide solid diamond nanobeam. Figure adapted from Ref. 51.

One option is to build an on-chip photon detector build directly into the diamond via doping. The biggest obstacles are that diamond has a small lattice constant, rigid structure, and a very large bandgap (5.5 eV).[54] Doping diamond to be *n*-type is still extremely difficult, and many species cannot be accommodated into the lattice via ion implantation, particularly at high enough densities to make it conductive without introducing extensive damage to the crystal structure and the color centers of interest. However, demonstrations of *p*-*i*-*n* diodes for electrically pumping NV centers in the *i*-region have been demonstrated, using both doped growth[55] and ion implantation.[56] It is

conceivable that similar techniques could be employed to make a sensitive photodetector out of diamond, but this is a daunting project.

A simpler but still challenging prospect is to generate a hybrid material structure where NVs in bulk diamond can be detected using a second, optoelectronic material whose technology as a photon detector is better developed. This hybrid scheme can work in two ways: (1) this second optoelectronic material can be deposited on diamond and processed into a detector on-chip or (2) the diamond waveguides can be transferred onto the optoelectronic material of interest. Chapter 4 of this dissertation discusses a scheme for detection of NV centers by transferring diamond waveguides onto top-down fabricated avalanche photodiodes in GaAs.

Chapter 2

Single Photovoltaic Junction of Conducting Polymer and an Inorganic Nanowire

2.1 Overview

As discussed in Chapter 1, bulk heterojunction solar cells are based on *p*-*n* junctions between conjugated polymers and semiconducting nanocrystals, nanowires, or fullerenes.[15,57-62] The mechanism of photocurrent generation in these heterojunctions is based on optical absorption in the polymer, the generation of tightly bound excitons in that component, and the diffusion of excitons to the semiconductor-polymer interface

where electron-hole pairs are separated.[63] The absorption properties of both components can be tuned to optimize photocurrent and minimize device thickness. Since the components are flexible and can be processed entirely in solution, bulk heterojunction solar cells are attractive candidates for applications involving flexible solar cells and photovoltaic "paint".[64] In this chapter, we present the fabrication and characterization of model devices consisting of a single P3HT segment contacting a single inorganic semiconducting nanowire. This simple geometry allows exciton generation and subsequent diffusion to be modeled. Together with this modeling, our photocurrent measurements allow us to calculate an efficiency of current output versus expected number of excitons that can diffuse to the interface. This charge collection efficiency (η_{cc}) is as high as 25%. However, this value varies greatly for neighboring devices prepared on the same chip. This suggests that the charge collection efficiency is highly dependent on the quality of the nanowire/polymer interface. This study provides a testbed of interface quality for the optimization of future bulk heterojunction solar cells.

2.2 Previous Investigations Using Single Heterojunctions

A strategy for investigating the charge separation and collection efficiency is to fabricate single NW/polymer heterojunctions, thereby eliminating complications arising from electrical shorting and incomplete hopping networks. A previous demonstration of this was achieved by chemically grafting a conjugated polymer layer on a single n-type ZnO nanowire to generate a core-shell structure,[65] and the external energy conversion efficiency was measured to be 0.04%. Similar in nature, a single P3HT-CdSe junction was generated through the use of electrodeposition into an anodic alumina template.[66]

After removal of the template, a single P3HT-CdSe device could be isolated and measured. However, the material quality was poor as evidenced by the *I-V* curves of the device in both dark and under broadband illumination and no attempt was made to quantify the device performance. Single P3HT-nanowire junctions have been generated elsewhere, but to our knowledge the charge separation efficiency of a hybrid photovoltaic device based on a single heterojunction has never been characterized.

2.3 Single CdS NW/P3HT Heterojunction Fabrication

The general scheme for characterizing a single hybrid photovoltaic device involving an inorganic nanowire and P3HT conjugated polymer is shown in Figure 2.1a. Unlike a bulk heterojunction solar cell, the NW and polymer strip are distinct entities that overlap in a well-defined manner, and their sizes and morphology can be accurately characterized via standard techniques such as atomic force microscopy (AFM) and scanning electron microsopy (SEM). The photocurrent generated by such a device can be conducted through the nanowire and polymer without concern for hopping between different nanocrystals, shorting each component to the opposite electrode, or carrier blocking layers, which complicate the efficiency calculations of bulk heterojunctions. In principle, this device can serve as a model heterojunction and its efficiency can be scaled to represent the ultimate performance of a bulk heterojunction device.

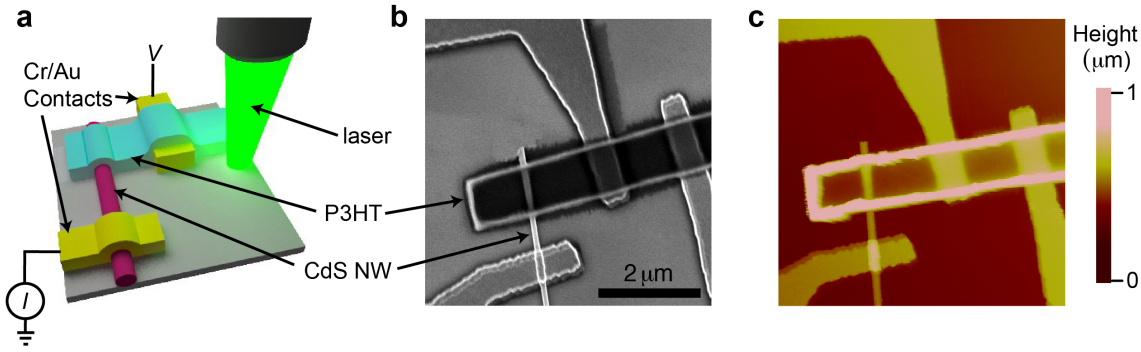

Figure 2.1 | Single CdS/P3HT heterojunction fabrication. (a) Device schematic for measuring a single heterojunction using a scanning photocurrent imaging setup. **(b)** SEM image of a representative device incorporating a single CdS NW and a P3HT strip. **(c)** AFM image of the same device as in (b).

The CdS NWs used in this experiment are synthesized using a solution-liquid-solid method with Bi nanoparticles as catalysts,[67] and are typically 50-100 nm in diameter and 2-4 μm in length (Fig. 2.1b). The NWs are suspended in anhydrous hexane and dispersed on silicon chips covered with 300 nm of SiO_2. They are electrically contacted using conventional electron-beam lithography and metallization with Cr/Au (30 nm/120 nm). A window for the P3HT strip is also defined using electron-beam lithography. The polymer strip is typically 40-100 nm thick in the center and has a 400 nm thick "frame" as determined by AFM (Fig. 2.1c). The devices are quickly wire-bonded and transferred to a measurement setup with flowing dry nitrogen gas to avoid water uptake, which can degrade the polymer.[68] This process could be altered to include fabrication-based passivation schemes, such as low temperature ALD,[69] directly on the heterojunction, but this would also complicate the modeling.

2.4 Single Heterojunction Dark Current-Voltage Characteristics

The CdS NWs and P3HT strips both exhibit linear (or nearly linear) current-voltage (*I-V*) characteristics (Fig. 2.2a-b). The CdS NWs are highly conductive (~10 kΩ), while the P3HT strips are more resistive (~2 GΩ per μm in length). Four-probe resistance measurements show that the contact resistances of both the P3HT strips and the CdS NWs are at least ten times smaller than the resistance across the CdS/P3HT junction. Our gate-voltage studies demonstrate that the P3HT exhibits a strong *p*-type field effect (Fig. 2.2b), from which the charge carrier density and mobility are estimated to be 10^{16} cm^{-3} and 10^{-2} cm^2/Vs, respectively. The highly conductive CdS NWs do not exhibit a gate response. In the dark, the P3HT/CdS-NW junction exhibits the desired rectifying behavior, with a voltage threshold of 0.5-1.0 V at forward bias (Fig. 2.2c).

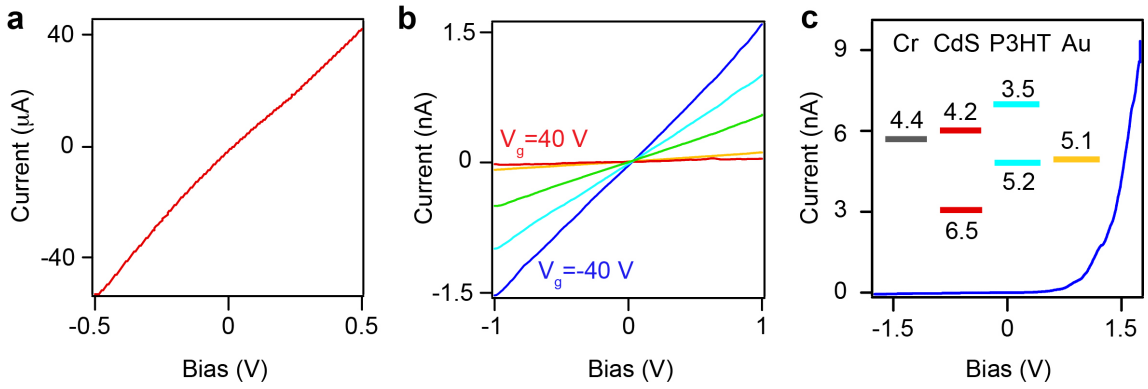

Figure 2.2 | Current-voltage characteristics of CdS nanowires and P3HT strips in dark. (a) A CdS NW showing near-linear behavior as a function of source-drain bias. **(b)** Back-gate dependent *I-V* curves of a segment of *p*-type P3HT polymer (V_G = -40, -20, 0, 20, 40 V). **(c)** *I-V* curve for a CdS-P3HT heterojunction in dark. Inset: energy band diagram with material band energies in eV with vacuum as reference.

2.5 Scanning Photocurrent Imaging of a Single Heterojunction

The optical response of a single heterojunction is characterized using a homebuilt scanning confocal microscope (Fig. 2.1a).[70,71] A diagram of the confocal microscope configuration is shown in Appendix I. Two separate light sources are used for these experiments: the first is a 532 nm continuous wave (CW) diode laser (Coherent), and the second is a picosecond pulsed supercontinuum laser (Koheras/NKT) with an acousto-optic tunable filter, allowing the illumination wavelength to be tuned from 470 to 750 nm. The incident light is focused to a diffraction-limited spot using a microscope objective lens (Olympus 100×, NA=0.8). The average light intensity incident on the device is ~1000 W/cm^2. The laser spot is scanned on the device by a computer-controlled x-y galvanometer while the reflected laser power and electrical current are simultaneously recorded.

The zero-bias photocurrent image (Fig. 2.3a) demonstrates that current is collected only when the laser spot is directly incident on the NW/polymer interface. This result was consistent for all of the devices studied (>100 devices). When the illumination energy is below the CdS absorption edge, the measured photocurrent must be due to exciton generation in the P3HT. Only excitons generated near the junction have a high probability of diffusing to the interface, where they can separate into free electrons and holes. Away from the interface, the electric field is too weak to separate the tightly bound excitons.[63] The exciton diffusion length (L_{ex}) has been measured to be ~2.5-10 nm for P3HT.[9,10,72] The extent of the photocurrent spot in Fig. 2.3a is therefore due to the laser's finite spot size and is not a measure of L_{ex} in the P3HT.

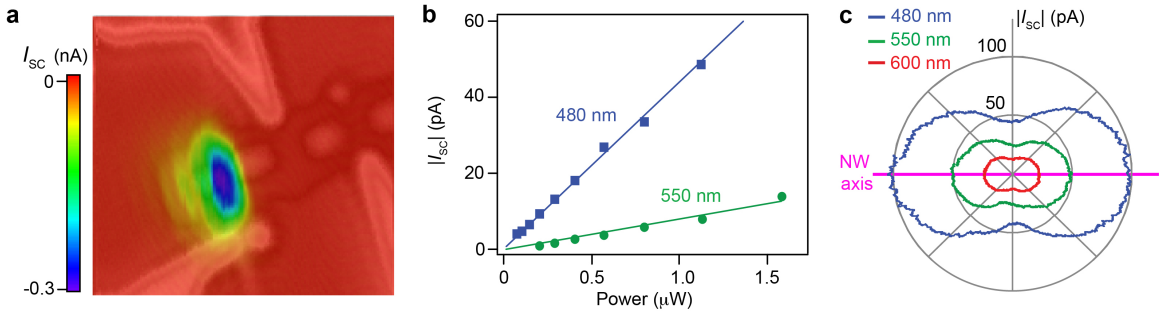

Figure 2.3 | Short circuit current of a CdS/P3HT junction. (a) Overlap of the simultaneously-cllected reflection and photocurrent images of the same device as in Fig 2.2b-c taken at zero bias. **(b)** Linear power dependence of the short circuit current of a different device from (a) with excitation energies both below (550 nm) and above (480 nm) the bandgap of CdS. **(c)** Polarization dependence of I_{sc}. The orientation of the NW is horizontal and the excitation power is 1.1, 1.6, 1.9 μW at 480, 550, 600 nm respectively.

The value of $|I_{SC}|$ appears to have a linear relationship—at least for the powers investigated—with the incident photon energy (Fig. 2.3b), both below (550 nm) and above (480 nm) the CdS bandgap, which is ~520 nm for bulk crystals. One final note about these laser measurements is that the polarization of the incident laser spot is important. The magnitude of the polarization dependence of incident light with respect to the NW axis (Fig. 2.3c) is consistent with the geometric dielectric contrast between the NW and the surrounding polymer.[73] As a result of this dependence, the polarization of the laser was always aligned along the nanowire axis to maximize the photocurrent and also mitigate device-to-device variations from this effect.

2.6 Modeling Charge Collection Efficiency

Since these single heterojunctions have a photovoltaic response, the next step is to model the fundamental ability of the organic/inorganic interface to separate excitons and to establish an upper bound to the overall energy conversion efficiency. In particular we want to quantify the ratio of collected experimental current to the expected flux of

excitons from the two components reaching the interface. With this aim, we define the charge collection efficiency η_{cc} to be:

$$\eta_{cc} = \frac{|I_{SC}|}{q(F_{ex,\,P3HT} + F_{h,CdS})}$$

where $F_{ex,P3HT}$ is the exciton flux diffusing through the interface from the P3HT and $F_{h,CdS}$ is the flux of holes diffusing through the interface from the CdS. The reason why the second term in the denominator is $F_{h,CdS}$ instead of $F_{ex,CdS}$ is discussed below.

To obtain $F_{ex,P3HT}$ for a particular NW/polymer junction, a 3D finite-difference time-domain (FDTD) simulation is employed to obtain the electrical field distribution in the device when it is illuminated with a diffraction-limited spot (Fig. 2.4a). The physical geometry used in the FDTD simulation is determined by AFM of the device (NW diameter, polymer thickness and shape, etc.). In addition to the physical structure of each device, the optical constants of the materials need to be included in the simulation. The complex refractive indices of CdS are from references[74] and *n, k* values for P3HT were obtained from spectroscopic ellipsometry and absorption spectra of typical P3HT films. From the FDTD the electric field profile, $E(x,y,z)$, for each device was used to calculate the exciton generation rate, $G_{P3HT}(x,y,z)$, in the P3HT as a function of position:

$$G_{P3HT}(x,y,z) = \frac{\left(\frac{c_0 \varepsilon_0 n_{P3HT} |E(x,y,z)|^2}{2}\right)\alpha_{P3HT}}{\left(\frac{hc_0}{\lambda_0}\right)}$$

where α_{P3HT} is the absorption coefficient and n_{P3HT} is the refractive index in P3HT and both parameters depend on the wavelength. This spatial map of exciton generation in the

P3HT, along with the location of the interface, can be ported into COMSOL finite element software. It is then possible to calculate the rate of excitons in the P3HT reaching the interface by solving the diffusion equation of the form:

$$D\nabla^2 c + G - \frac{c}{\tau} = 0$$

where c is the exciton concentration, G is the exciton generation rate mentioned above, τ is the exciton lifetime, and $D = L_{ex}^2/\tau$ is the exciton diffusion coefficient in P3HT.

In order to solve this diffusion equation there are two important assumptions. First, the interface is assumed to be perfectly absorptive, and mathematically this condition is equivalent to c=0 at the interface, since the boundary layer length for this system is much smaller than the exciton diffusion length.[75] Therefore, solving the diffusion equation with this boundary condition will give the rate at which excitons reach the interface. Second, since there are differing reports of the diffusion coefficient D in P3HT, two sets of diffusion lengths and exciton lifetimes are considered: (τ = 0.3 ns, L_{ex}=5.3 nm)[9] which gives $D = 9.4\text{x}10^{-8}$ m^2/s and (τ= 0.4 ns, L_{ex}=8.5 nm)[10] which gives $D = 1.8\text{x}10^{-7}$ m^2/s. The exciton flux $F_{ex,P3HT}$ into the interface is then, $\int_s n \cdot \nabla c \, ds$, where n is the normal vector at the interface and s is the interfacial area.

To obtain the CdS NW contribution to the expected photocurrent, a similar process can be performed as for the P3HT. However, the exciton binding energy in CdS is less than the thermal energy, therefore electron-hole pairs in CdS are very weakly bound or unbound,[76] thus instead of a $F_{ex,CdS}$ term in the deonominator of η_{cc} above it is $F_{h,CdS}$. Photogenerated minority holes in the CdS have a long diffusion length of ~0.7 μm in bulk.[77] Since this length exceeds the NW diameter for all pump wavelengths above the

bandgap of CdS, nearly all the photons absorbed in the CdS lead to holes that diffuse to the interface and contribute to $F_{h,CdS}$. Overall this implies that photogenerated holes are readily swept out of the NW at the CdS/P3HT interface. This is in accord with the measurements in Figure 2.4b (left axis) as the photocurrent increases considerably when the illumination energy is greater than the CdS bandgap (~520 nm).

Our simulations enable I_{SC} to be partitioned based on the material in which the photons were absorbed. When the excitation energy is below the CdS bandgap, I_{SC} is due to excitons diffusing to the interface from the polymer. Above the bandgap, the free carriers generated in the NW dominate I_{SC} (Fig. 2.4b, right axis).

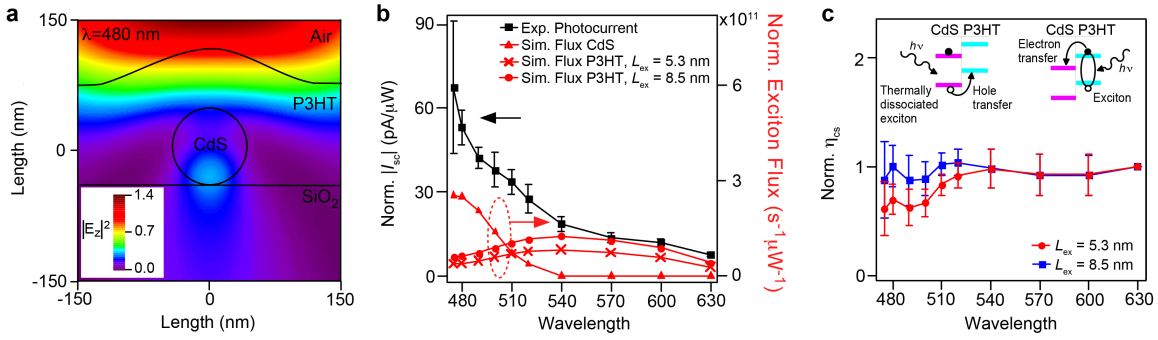

Figure 2.4 | Estimating the Charge Collection Efficiency in CdS/P3HT heterojunctions. (a) Two-dimensional cross-section of the electric field profile of a diffraction limited laser spot on a CdS NW/P3HT strip simulated via FDTD. **(b)** Left axis, typical experimental zero-bias photocurrent of a NW/polymer device normalized by the power spectrum of the incident laser. Right axis, the simulated power-normalized exciton flux reaching the NW/polymer interface at various excitation wavelengths. The red cross and red triangle curves assume a different exciton diffusion length in P3HT of 5.3 nm and 8.5 nm, respectively. **(c)** Averaged charge collection efficiencies (η_{cc}) for 10 devices where at each wavelength the efficiency is normalized to the value at 630 nm. The red and blue curves assume an exciton diffusion length in P3HT of 5.3 nm and 8.5 nm, respectively. The error bars represent the device-to-device variation. Inset: Two diagrams illustrating the majority charge carrier generation mechanism.

The η_{cc} of our best devices were as high as 9% (assuming L_{ex} is 5.3 nm). Particularly interesting about the charge collection efficiency is that devices prepared on the same chip can have vastly different efficiencies. For example, in a set of ten devices prepared on the same chip, with identical polymer/electrode geometries, η_{cc} varied from 0.2 to 1%. This large device-to-device variation is of particular importance because it suggests that subtle differences at the polymer/NW interface can dramatically change the charge collection efficiency. This sensitivity of individual heterojunctions is difficult to capture in ensemble devices.

In spite of these large device-to-device variations, the shape of η_{cc} does not sensitively depend on the excitation wavelength (Fig. 2.4c). Below the bandgap of CdS, the normalized η_{cc} is flat within the error bars. Our finding is in agreement with the fact that the hot exciton relaxation time in conjugated polymers has been estimated to be ~100 fs,[78] much faster than the time that excitons take to diffuse to the P3HT/CdS interface. Accordingly, nearly all the excitons at the interface have relaxed to their ground state, and there is no wavelength dependence to their dissociation.

2.7 Light-Dark *I-V* Curves of a Single Heterojunction

The most troubling issue for these single CdS-P3HT heterojunctions is that the magnitudes of the overall charge collection efficiencies are low. The simulated photocurrent from these devices is far larger than would generally be expected just by computing V_{OC}/R_{P3HT}. In order to further investigate device performance, we performed current versus voltage sweeps for these devices under laser illumination.

The *I-V* sweeps were measured after centering the laser spot on the NW/polymer junction. An example trace is shown in Figure 2.5a yielding a short-circuit current (I_{SC}) of -300 pA, and an open-circuit voltage (V_{OC}) of 0.82 V. These quantities vary from device to device, $|I_{SC}|$ ranging from tens to hundreds of pA and V_{OC} ranging from 0.7-0.8 V. The *I-V* curves of these single NW/polymer devices under illumination have a modified overall shape from those of typical ensemble hybrid solar cells.[15] There are three noticeable qualitative differences from the bulk heterojunction *I-V* traces. First, under forward bias, the large polymer resistance limits the current above the voltage threshold, so that it increases linearly instead of exponentially. Second, the conductivity in forward bias increases slightly when under illumination. The third and most prominent feature is that the reverse bias current does not saturate.

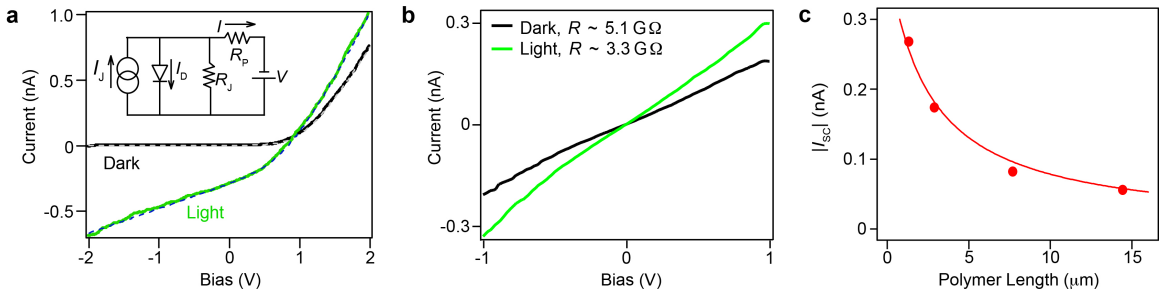

Figure 2.5 | Current-Voltage curves for a CdS/P3HT junction with incident 532 nm laser. (a) Comparison of heterojunction *I-V* characteristics in the dark and under the illumination of a 532 nm CW laser with a power of ~0.8 μW (or ~700 W/cm^2). The solid lines are the experimental data and the dashed lines are the fits using the equivalent circuit model. Inset shows an equivalent circuit of the NW/polymer device. **(b)** *I-V* curve for a bare P3HT strip with in the dark and illuminated with a diffraction-limited spot intensity of ~2000 W/cm^2. **(c)** A plot of short circuit current as a function of polymer length for a different single heterojunction device than (a) with multiple polymer electrodes.

The change of conductivity for the CdS/P3HT heterojunction in forward bias can be explained by the slight photoconductivity of the P3HT at the generally high intensities

used for this experiment. For most of the devices investigated, this increase in conductivity is 10-20% at illumination intensities near 500 W/cm^2. In a control experiment consisting of only a single P3HT strip, with a diffraction-limited spot in the center of the strip, the photoconductivity is 50% greater than the dark conductivity under an illumination intensity of ~2000 W/cm^2 (Fig. 2.5b). This photoconductivity may be due to the small probability of free charge carrier generation, which occurs with an efficiency of $<10^{-2}$ in MEH-PPV.[79] Alternatively, it may be due to chemical impurities in the P3HT.[80] Using the absorption coefficient for P3HT (~1.5x10^5 cm^{-1} at 532 nm), the measured laser intensity, and the exciton lifetime of 0.3 ns,[9] the density of light-induced carriers in the P3HT can be estimated to be 10^{16}-10^{17} cm^{-3}. This density is close to the dark-state hole concentration (10^{16} cm^{-3}) implied by the back-gate response of the P3HT.

Under reverse bias, the current is dominated by light-induced charge leakage. Quantitatively, our devices can be modeled with a simple equivalent circuit[81] (Fig. 2.5a inset), which consists of a current source I_J shunted by a diode and a junction resistance (R_J), all in series with a polymer resistance (R_P). This can be represented mathematically as:

$$I = -I_J + I_0(e^{q(V-I\cdot R_P)/AkT} - 1) - (V - I\cdot R_P)/R_J$$

where I is the current through the load, I_0 is the saturation current, q is the electron charge, A is the ideality factor, k is Boltzmann's constant, and T is the temperature. The measured I-V curves agree with fits obtained using this equivalent circuit model (Fig. 2.5a dashed lines): yielding $I_0 = 2\times10^{-14}$ A, $A = 4$, $R_P = 1.2$ GΩ in dark and 0.9 GΩ under light, $R_J = \infty$ in dark and 5 GΩ under light, and $I_J = 0.35$ nA.

The most obvious experimental parameter to sweep in order to verify the equivalent circuit model is the polymer resistance (R_P). In fact, it is simple to use multiple polymer contacts at different distances from the same heterointerface and plot the short circuit current as a function of the polymer resistance. According to the equivalent circuit model, there should be a simple current divider relationship for the short circuit current (because I_0 is very small and can be neglected at V=0): $I_{sc} \cong I_J R_J / (R_J + \rho L_P)$, where ρ is the polymer resistance per unit length. The experimental data can be fit reasonably well using this simple equation (Fig 2.5c).

2.8 Understanding Power Dependence of *I-V* Curves

The equivalent circuit seems to correctly describe the experimental data in Figure 2.5c, but in order to understand the physical meaning of this shunting junction resistance, R_J, it is essential to investigate the power dependence of the *I-V* curves. As the illumination intensity is increased (Fig. 2.6a), the reverse-bias resistance decreases considerably.

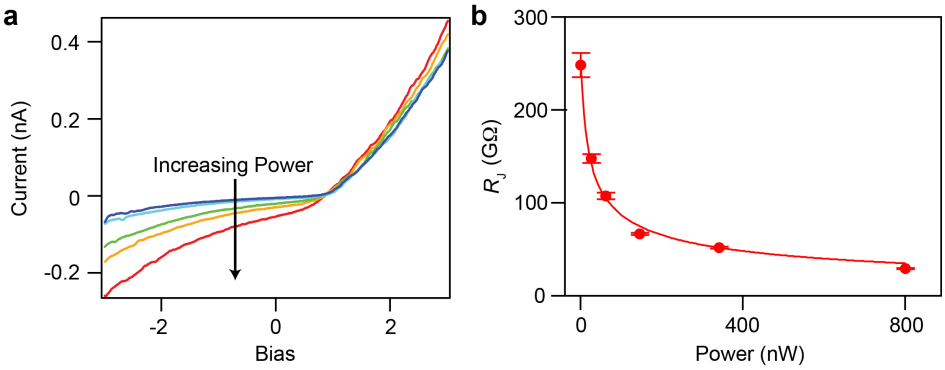

Figure 2.6 | Power dependence of a CdS/P3HT junction with incident tunable laser. **(a)** *I-V* characteristics of a device at various light intensities with a wavelength of 550 nm. **(b)** R_J plotted versus incident power. R_J was extracted from the slope of the linear part (-0.5 V to 0 V) of the *I-V* curves under reverse bias in (a). The fit is of the form $R_J = R_0(1 - e^{-B/\sqrt{P}})$.

A physical interpretation of the junction resistance is that heterojunction is a source of photogenerated carriers, which reduce the depletion width in P3HT and enable free carriers to tunnel back through the depletion region and recombine. A simplistic model of this can be given by assuming that the tunnel barrier is triangular in shape, the probability (Θ) of a carrier tunneling across a triangular barrier[82] is given by:

$$\Theta \propto e^{-\frac{4}{3}\frac{\sqrt{2qm^*\phi_B}}{\hbar}W}$$

where q is the charge, m^* is the effective mass, ϕ_B is the potential barrier height and W is the depletion width. The depletion width is related to the carrier concentration n (holes specifically in the P3HT) and the incident power P by $W \propto \frac{1}{n^{1/2}} \propto \frac{1}{P^{1/2}}$. The junction resistance is proportional to the probability that the carrier *doesn't* tunnel, $R_J \propto 1-\Theta$. Therefore, the substitution of the depletion width as a function of power yields $R_J = R_0(1-e^{-\frac{B}{\sqrt{P}}})$, where B is a parameter that depends on the barrier height and P is the excitation power. A general fit of this form is shown for the R_J values extracted as a function of incident power in Figure 2.6b.

The power-dependence in Fig. 2.6a allows us to estimate the extent of light-induced recombination after charge separation. More specifically, it allows the junction current (I_J) to be extracted from the *I-V* curve. I_J can be interpreted as the actual current output of the heterojunction, and the leakage current from recombination is that which flows through R_J. As an example, for the device shown in Fig. 2.3a, I_J is 16% larger than I_{SC}. Devices that are illuminated with a lower light intensity exhibit much less leakage current.

Furthermore, the change in R_J with incident power is unlikely to be caused by laser heating because the laser power is relatively low and the SiO_2 substrate behaves as a heat sink. The rise in device temperature can be estimated as $\Delta T = \frac{P \cdot d}{\kappa_{SiO_2} S} < 1$ K, where $P = 1$ μW is the maximum laser power, $d = 300$ nm is the SiO_2 substrate thickness, $\kappa_{SiO2} = 1.4$ W/m K is the thermal conductivity of SiO_2, and $S \sim (500 \text{ nm})^2$ is the approximate laser spot size.

2.9 Reducing the P3HT resistance in CdSe/P3HT single heterojunctions

The most troubling issue for these single CdS-P3HT heterojunctions is that the overall magnitude of charge collection efficiency is low. The simulated photocurrent from these devices is far larger than would generally be expected by merely computing V_{OC}/R_{P3HT}. Thus for the input laser powers used thus far (50 nW to 1 μW) the conjugated polymer resistance is too high and behaves as a current-limiting resistor. This mistake was somewhat unavoidable, as these higher powers were necessary to obtain I_{SC} signal for most devices (for example, $|I_{SC}|$ when pumping with 550 nm light and 200 nW is just a few pA in Figure 2.3b).

Initially we attempted to use R_p dependence to extract an ideal I_{SC}, via fitting as in Figure 2.5c. Unfortunately, small deviations in the fit led to huge changes in the extracted photocurrent at small polymer resistance. In addition, there were many attempts made to reduce the length between the CdS nanowire and the P3HT electrode using the previously described fabrication methodology; however, nearly all the devices exhibited shorting

between the nanowire and polymer electrode, the ones that were not shorted had issues with P3HT morphology.

Therefore, a modified experimental scheme should be employed to reliably reduce the polymer length by an order of magnitude. It would be equally valuable to achieve more photocurrent for a given input laser power, which would allow the power to be reduced and yet still achieve high signal-to-noise for the short circuit current. The schematic to achieve both of these aims is shown in Figure 2.7.

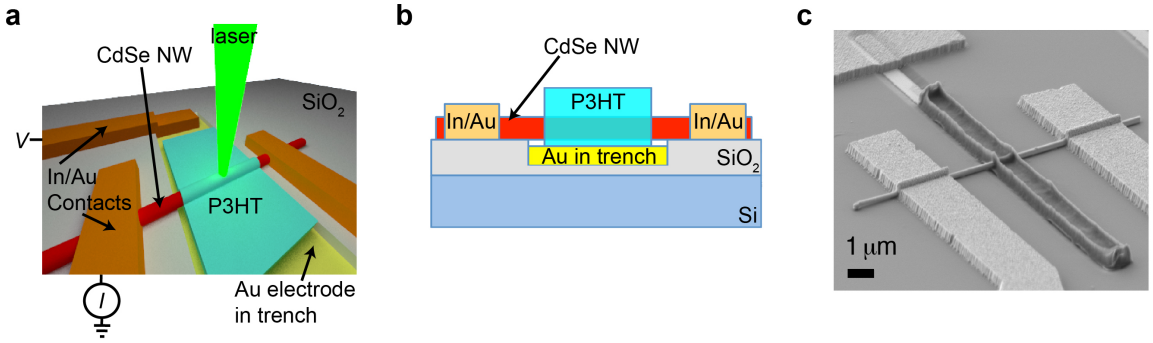

Figure 2.7 | Modified scheme for CdSe/P3HT heterojunctions. (a) Device schematic for measuring a single heterojunction using a scanning photocurrent imaging setup. The CdSe nanowire is suspended over a shallow trench with a gold electrode underneath. The polymer fills in the gap between the nanowire and the trench electrode. **(b)** Cross section schematic along the axis of the nanowire. **(c)** SEM image of a representative device incorporating a single CdSe NW and a P3HT strip, the depth of the trench is ~90 nm.

The general device operating principle for the CdSe-P3HT heterojunction is identical to that of the CdS-P3HT from before. The two main differences are that (1) the CdS nanowire has been swapped for CdSe, which has a smaller bandgap of ~710 nm so that it contributes more to the photocurrent for a given laser power, and (2) the polymer length has been shortened by an order of magnitude by suspending the nanowire over a shallow

trench electrode and having the flowable polymer fill in the small gap (<100 nm) during the spinning process.

The CdSe NWs used in this experiment are synthesized using a vapor-liquid-solid method with Au nanoparticles as catalysts and indium as the *n*-type dopant introduced during the growth.[83] The nanowires are typically 50-100 nm in diameter and 5-20 μm in length (Fig. 2.7c). The measurement substrate consists of a silicon chip with 300 nm of thermal SiO_2 and 100 nm deep trenches that are etched into the oxide. Both the CdSe NWs and the bottom electrodes in the trench are electrically contacted using conventional electron-beam lithography and metallization with In/Au (15 nm/285 nm) to achieve Ohmic contact. A test measurement is performed between the nanowire and the trench electrode to ensure they are not shorted prior to spinning of the P3HT.

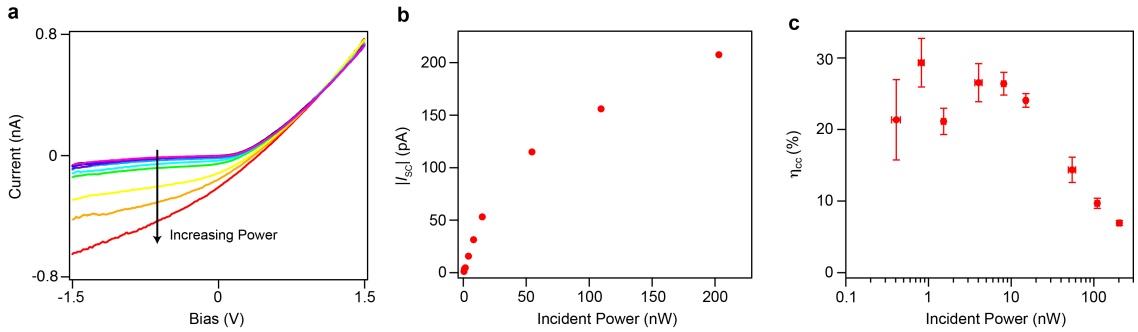

Figure 2.8 | Optoelectronic properties of a CdSe/P3HT heterojunction using a 532 nm laser. (a) *I-V* characteristics of a typical device at various laser power (in order of increasing power: dark, 0.4, 0.8, 1.5, 4, 8, 15, 54, 109, 203 nW). **(b)** The short circuit current for each of these curves in (a). Notice the two seemingly linear regimes of $|I_{SC}|$ both below and above ~50 nW. **(c)** A plot of the charge collection efficiency as a function of incident power with the assumption that L_{ex} for P3HT is 5.3 nm.

The light and dark *I-V* curves of these modified devices look very similar to that of the CdS nanowire-based devices shown in Figure 2.6a when pumped at 532 nm.

However, the plot of the short circuit current as function of incident power (Fig 2.8b) is quite different from before in Figure 2.3b. Instead of being linear throughout the measurement range, there appear to be two different linear regimes below and above ~40 nW. This might be expected as the polymer resistance limits the current for higher intensities. If we perform a similar calculation of the charge collection efficiency as before (substituting in optical constants for CdSe[84]) for this device, we can see that below 40 nW the efficiency seems to saturate near 25% (Fig. 2.8c). Furthermore, for the lower power range, the external quantum efficiency (electrons collected/photons incident) is ~1%.

Unfortunately, the tunable laser used for the wavelength dependence in CdS-P3HT devices was under repair for a significant amount of time, so there are no wavelength dependence measurements for these CdSe-P3HT devices. However, it might be possible to draw some general qualitative conclusions from these modified P3HT-CdSe devices and apply them to the earlier system. At the very least, it confirms that the actual charge collection efficiency would be much higher if investigated with shorter P3HT lengths. If one assumes that the general trend for $|I_{SC}|$ in the absence of a current-limiting polymer resistance is equal for both systems, then for the best CdS-P3HT devices (η_{cc} = 9% for P=800 nW) the charge separation efficiency could be well in excess of 50%. This is quite close to the value of 60% reported Mihailetchi *et al*. in fullerene-based bulk heterojunctions.[11]

2.10 Outlook

Our study of single polymer/NW heterojunctions provides a new approach to characterizing interfacial charge separation and transport in hybrid photovoltaic devices. The most significant conclusion that can be applied to bulk heterojunction solar cells is the high variation in efficiency between devices on the same chip. This high degree of variation suggests that the quality of the interface between the donor and acceptor is critical to realizing higher efficiencies. Future studies on NW/P3HT junctions may be able to address how the interface affects the charge separation efficiencies more rigorously. Particularly interesting would be to apply our methodology to analyze the charge collection efficiency of grafted polymer/NW heterostructures[65] in order to directly compare the interface quality of spinning P3HT versus chemical grafting. In doing so, we may be able to controllably improve device performance and device-to-device variability in both model and bulk heterojunction solar cells. This idea could even be extended to using these types of devices as a testbed for optimizing electron acceptor/donor interfaces.

Chapter 3

On-Chip Electro-Optical Generation of Single Surface Plasmon Polaritons

3.1 Overview

Integrated quantum optical circuits require efficient generation and collection of single photons. Typically, single photons are generated by focusing light onto a quantum emitter with a high numerical aperture objective and routed using far field collection into a single optical mode, a process that is highly inefficient.[25,85,86] Nanowire optoelectronic devices are a promising platform for scalable quantum optical circuits because they can

waveguide light at sub-micron dimensions, and have been shown to generate and detect light efficiently with small device footprints.[87-90] In this chapter, we demonstrate an integrated device, in which a quantum emitter is excited by an on-chip single-nanowire light-emitting diode (LED), and its emission is routed into single surface plasmon polaritons (SPPs) along a metallic nanowire plasmonic waveguide. Plasmonic nanowire waveguides serve to collect single photons efficiently as SPPs, which can then be used for broadband, enhanced light-matter interaction. Our electro-optic single plasmon source presents a step toward a wide range of applications in quantum information processing, such as single photon transistors.[91]

3.2 Fabrication Scheme for an Electrical Single Plasmon Source

The hybrid device employed in this experiment is shown in Figure 3.1. It involves a single photon emitter (colloidal CdSe quantum dot), which is in very close proximity to a plasmonic waveguide (Ag nanowire), and the emitter is pumped with an on-chip LED (GaN-based NW). The details of the fabrication process are given in Appendix A.II.2.

Each of the components in this hybrid geometry was selected because of its complimentary optoelectronic characteristics. Colloidal quantum dots were chosen as the single photon source for their high quantum yield and wide spectral tunability.[92] The single photons from the QD are collected by the plasmonic waveguide placed in the near field of the quantum dot, generating single SPPs.[26] Chemically-grown silver nanowires are used as the plasmonic waveguides, which are highly crystalline and defect-free, leading to relatively low transmission losses,[93,94] and the absence of scattering center defects prevents LED radiation from coupling into SPPs. A GaN-based NW LED is used

to pump the QD for three reasons. First, the high absorption coefficient for the QD in the blue wavelength range increases the pumping efficiency. Second, the blue emission from the LED is spectrally distinct from the red quantum dot fluorescence making it easier to distinguish the QD emission. Third, an SPP with energy close to the surface plasmon resonance of the material (λ_{SP} = 405 nm for silver) will suffer higher propagation loss due to the increased electron-phonon and electron-electron scattering.[95] Thus any blue radiation that couples into an SPP is spectrally filtered as the plasmon propagates along the waveguide (Fig. 3.2c). Finally, the T-shaped geometry of the two nanowires in Figure 3.1a is intentional. Orienting the silver nanowire normal to the LED nanowire axis maximizes the photon-SPP momentum mismatch, thereby minimizing the coupling between LED emission and SPPs.

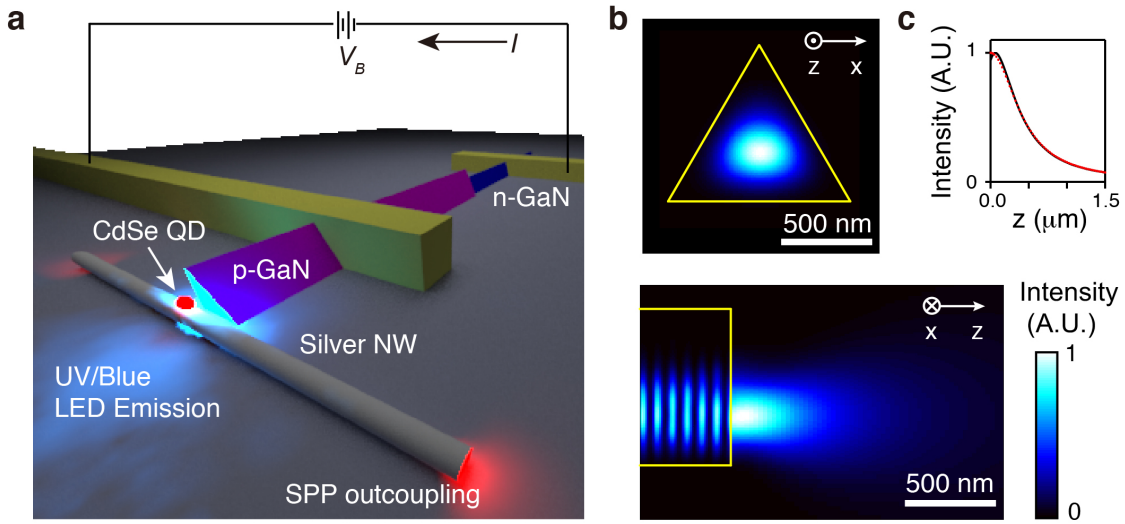

Figure 3.1 | Scheme for electro-optical generation of single plasmon polaritons (a) Schematic diagram of electro-optical generation of single photons and subsequent coupling to SPPs. **(b)** FDTD simulation of $|\mathbf{E}|^2$ for the fundamental photonic mode (λ = 410 nm) propagating along a GaN nanowire. Cross-section views are shown for its end facet (top panel) and its vertical axial plane (bottom panel), and the location of the GaN is outlined in yellow. **(c)** $|\mathbf{E}|^2$ along the propagation direction of the GaN nanowire emission (black line) and an ideal Gaussian beam with divergence $\Theta = 20.7^o$ and λ = 410 nm (red dashed line). The nanowire end facet is located at z = 0.

The blue LED is fabricated from a coaxial (core/shell/shell) *n*-GaN/*i*-$In_xGa_{1-x}N$/*p*-GaN nanowire with $x \approx 0.1$. The intrinsic $In_xGa_{1-x}N$ has a band gap of ~3 eV (410 nm), which is tuned by varying the indium concentration. Geometrically, the nanowire has a length up to 40 μm and an equilateral triangular cross section of ~1 μm per side. The nanowire has a large index of refraction ($n_{GaN,\ 410\ nm} = 2.54$)[96] and supports many guided photonic modes. According to finite-difference time-domain (FDTD) simulations, the fundamental mode emits from the end facet of the nanowire as a Gaussian beam with ~ 20° divergence (Fig. 3.1b). A colloidal quantum dot placed within 400 nm distance of the end facet of the LED, therefore, experiences at least half of the maximum excitation intensity as shown in Figure 3.1c.

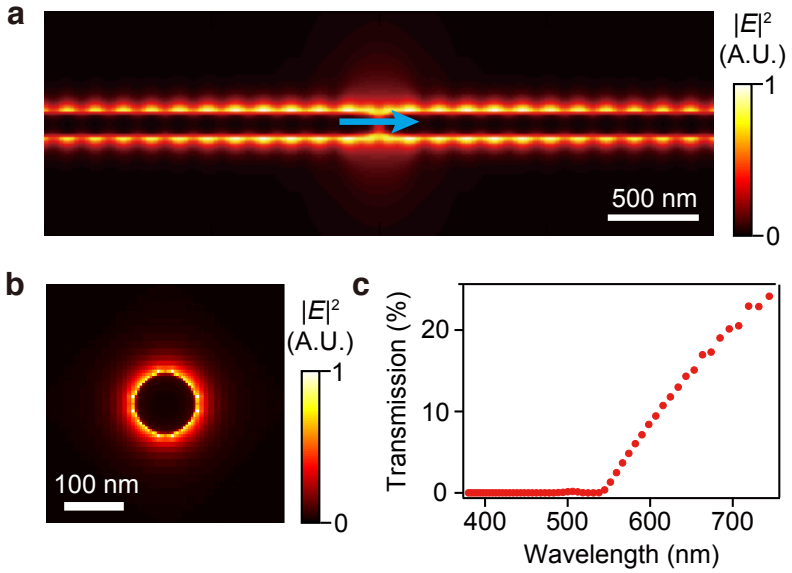

Figure 3.2 | Dipole source SPP propagation simulations and spectral filtering (a) Finite-difference time-domain (FDTD) simulation of the electric field intensity ($|\mathbf{E}|^2$) along a silver nanowire, with a radiating point dipole source (λ = 650 nm, indicated by the blue arrow) placed in the near field of the nanowire. **(b)** The electric field intensity ($|\mathbf{E}|^2$) distribution for the fundamental surface plasmon polariton mode propagating along a 100-nm-diameter silver nanowire. **(c)** Transmission spectrum of the mode after 5 μm, significant transmission is only observed for $\lambda > 550$ nm.

For our FDTD simulations (Fig. 3.2b-c), the silver nanowire is modeled as a 100-nm-diameter silver cylinder embedded in a medium of $\varepsilon = 2.16$ (SiO_2). The dielectric function of silver is adapted from Johnson and Christy.[95] Near one end of the nanowire, the fundamental TM mode ($m = 0$), which is the only propagating surface plasmon mode supported by a silver nanowire of this diameter, is injected along the nanowire's axis. The fraction of power transmitted through a plane placed 5 μm away from the mode injection plane is recorded for each wavelength and plotted in Figure 3.2c. The silver nanowire is long enough (> 10 μm) to eliminate significant reflection from the end facets.

3.3 Characterization of InGaN LED Emission

The scanning electron microscope (SEM) image of a blue nanowire LED device is shown in Figure 3.3a.[97,98] The *I-V* curve of the LED exhibits rectification characteristic of a *p-i-n* diode (Fig. 3.3b, black trace). As the forward bias exceeds the band gap (~3 eV) of the InGaN layer, current flows from the *p*- to *n*-region. Electroluminescence (EL) is generated through the radiative recombination of charge carriers injected into the InGaN layer, as depicted in the inset of Figure 3.3b, and the EL intensity is proportional to the driving current (Fig. 3.3b, blue circles). The emission spectrum collected from the nanowire end facet peaks around 410 nm (Fig. 3.3c), indicating that the NW emission is due to carrier recombination in the InGaN layer. Sub-bandgap emission at lower energies can be observed for measurements at room temperature, most likely resulting from surface trap states in the nanowire (Fig. 3.3c, red trace). The sub bandgap, so called "yellow band", emission is well known for GaN systems, and it arises from lattice defects

formed during the material growth. Previous reports suggest a deep trap located 1 eV above the GaN valence band edge is responsible for such emission.[99,100]

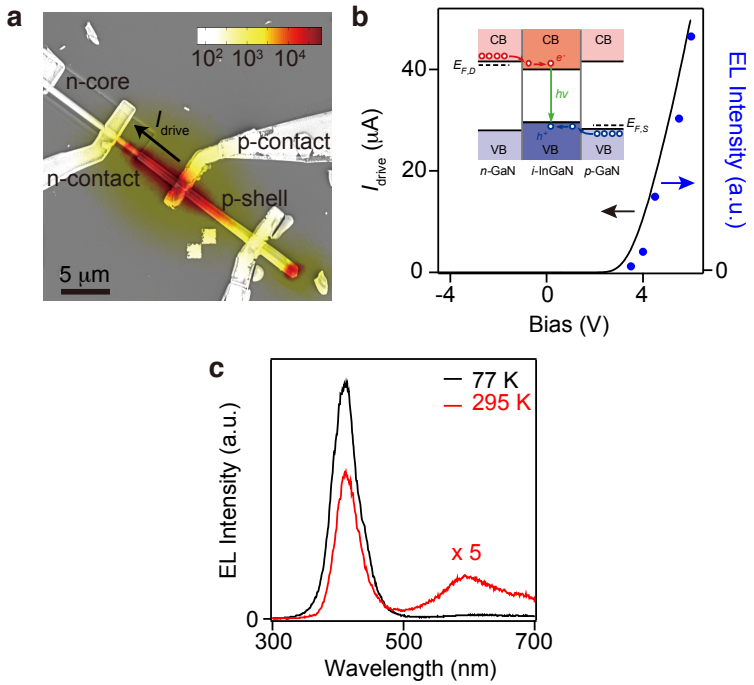

Figure 3.3 | Single nanowire light emitting diode (a) Scanning electron micrograph (SEM) of a typical LED device, overlaid with its electroluminescence image. **(b)** Current-voltage characteristics (black line) and electroluminescence versus applied bias relation (blue dots) of the device. Inset: Band diagram of the device and the light generation mechanism. **(c)** Electroluminescence from LED at room temperature (red line) and 77 K (black line). The room temperature curve has been multiplied by five times to show the sub-bandgap emission.

As the device is cooled to T=77 K, the sub-bandgap emission is significantly suppressed, greatly enhancing the color purity of the EL (Fig. 3.3c, black trace). For a typical LED driven at 100 μA, the power collected in the far field is a few nW. Considering the finite numerical aperture (NA) of the far-field optics and transmission losses due to absorption and scattering along the optical train, the quantum yield of the electroluminescence is ~0.1%. The low quantum yield is due to nonradiative

recombination at the trap states, which are also responsible for the below bandgap emission.[101] Light emission is not homogeneous across the *p*-*i*-*n* region, but concentrates near a few locations on the nanowire (Fig 3.3a). Due to the lower carrier mobility of the *p*-GaN,[98] most of the EL is generated around the *p*-type contact as current follows the shortest path in the *p*-type region. The bright spot at the end facet of the nanowire, as noted previously, is due to photonic guiding that arises from the large index of refraction of GaN.

3.4 Incorporation of Single CdSe Collodial Quantum Dots

When dispersed in the vicinity of the LED, colloidal CdSe/ZnS quantum dots (Invitrogen, 655 nm) can be optically excited by the LED electroluminescence. The spectrum collected from the end facet of one such diode is shown in the bottom panel of Figure 3.4, at 10 V bias. In addition to the blue EL from the *p*-*i*-*n* diode, a peak at 637 nm (1.947 eV) appears, originating from the electro-optical excitation of CdSe/ZnS quantum dots. At 77 K the emission peak blue shifts by 53 meV from the room temperature value of 655 nm (1.893 eV), this corresponds to a temperature coefficient $dE/dT = -0.25$ meV·K^{-1}. This blue shift has been previously reported and is explained by the temperature dependence of the bandgap of bulk CdSe, which has temperature coefficient $dE_g/dT = -0.28$ meV·K^{-1}.[102] The change in confinement energy due to the thermal expansion of the quantum dot is a comparatively small effect. The full-width at half-maximum (FWHM) linewidth of the quantum dot emission is about 45 nm, which is much broader than that of a single quantum dot,[103,104] confirming that the electro-optical emission results from an ensemble of quantum dots.

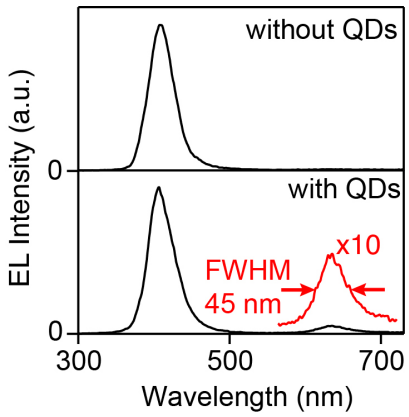

Figure 3.4 | Electro-optical excitation of colloidal quantum dots at *T*=77 K. Electroluminescence spectrum before and after a monolayer of CdSe/ZnS QDs is deposited on the LED device, showing the first exciton emission of the QDs (~650 nm). Red curve is the black curve multiplied by 10x to highlight the QD emission peak.

Figure 3.5a shows the SEM image of a typical fully assembled device. As proposed in Figure 3.1a, the Ag NW is placed at the end facet of the *p-i-n* nanowire diode, forming a T-shaped junction. Before silver nanowire deposition, the LED is coated with a conformal 250-nm SiO_2 layer by atomic layer deposition.[105] The SiO_2 layer is primarily used to raise the height of the silver nanowire so that it is located near the center of the end facet of the much taller *p-i-n* diode. The silver nanowires are aligned perpendicular to the LEDs by microfluidic alignment.[106] The high quality ALD layer also protects the diode from moisture and oxygen to prevent device degradation. Colloidal CdSe/ZnS quantum dots are deposited over the whole device by dispersing them in poly(methyl methacrylate) (PMMA) that is spun into a 30 nm thick film. The concentration of quantum dots is tuned to allow individual QDs to be optically resolvable after spinning, and on average only a single quantum dot is located at the end facet of the LED.

3.5 Optical Characterization of InGaN/Ag/CdSe hybrid system

After a full device is prepared (Fig. 3.5a), individual quantum dots are identified via scanning confocal fluorescence microscopy. Diagrams of the confocal configurations are shown in Appendix I. In Figure 3.5b, the confocal fluorescence image of the device is overlaid with its reflection image. Noise appearing on each bright fluorescence spot results from the blinking of individual quantum dots,[85] suggesting that the quantum dots are sparsely dispersed in the PMMA film. One quantum dot, marked by the green circle, is located close to both the LED end facet and the silver nanowire. The single photon statistics of the quantum dot are collected and confirm that it is a single photon source, as shown in the clear anti-bunching behavior (Fig. 3.5c). When the quantum dot is optically excited via a 532 nm laser, fluorescence is detected directly from the quantum dot as well as the end facets of the silver nanowire. This indicates that CdSe emission couples into SPPs and subsequently scatters into the far field at the end of the nanowire (Fig. 3.5d).

The blinking behavior evident in the QD emission timetraces provide additional evidence for the quantum dot–SPPs correlation. In the experiment, the quantum dot located at the T-shaped junction is optically excited with an external laser. Confocal Channel A collects fluorescence directly from the quantum dot, and Channel B collects fluorescence from SPPs scattering at the end facet of the Ag NW. As shown in Figure 3.5e, blinking of the direct emission from the quantum dot correlates in time with blinking from the plasmon spots, indicating that the emission from the ends of the Ag plasmon waveguide indeed originates from the QD.

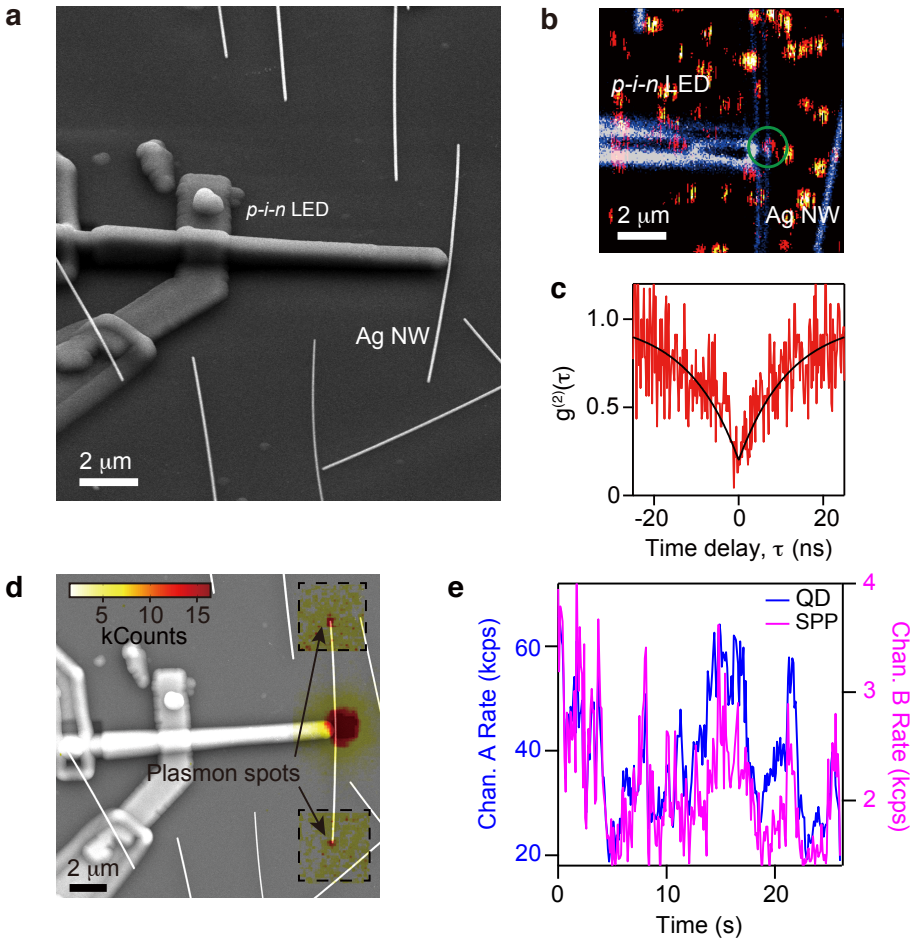

Figure 3.5 | Full device assembly and optical characterization. (a) SEM image of a fully assembled device. **(b)** Scanning confocal reflection image of the device (blue-white), overlaid with its confocal fluorescence image (red-yellow). The quantum dot is located at the T-shaped junction is marked by the green circle. **(c)** Second-order correlation function $g^{(2)}(\tau)$ of the quantum dot where the fit is shown in red. **(d)** Fluorescence image of the device, when the excitation laser is focused on the quantum dot. Signal around the plasmon out-coupling spots is enhanced by 10 times (enclosed by the dashed rectangles). The image is overlaid on an SEM image of the device. **(e)** Timetraces of fluorescence collected from the quantum dot at the T-shaped junction (Channel A, blue) and one end of the silver nanowire (Channel B, magenta), when the quantum dot is optically excited by the laser.

3.6 Electrical Pumping of Full Device at T=10 K

With the device fully characterized via external optical excitation, it is ready for electrical pumping via the LED. When current is driven through the nanowire LED,

emission that couples into SPP modes of the silver nanowire can be detected. Figure 3.6a shows an EL image taken at 7 V forward bias with a red longpass filter inserted in the optical path to block the dominant blue light. Light emission is not only detected from the diode but also at the end facets of the silver nanowire, indicating that emission from electro-optically pumped quantum dots couples to SPPs. It is important to note that the plasmon spots disappear after the removal of the quantum dots by solvent stripping. This demonstrates the SPPs arise from the near-field coupling between the quantum dot and the silver nanowire rather than direct coupling of sub-band gap emission from the diode.

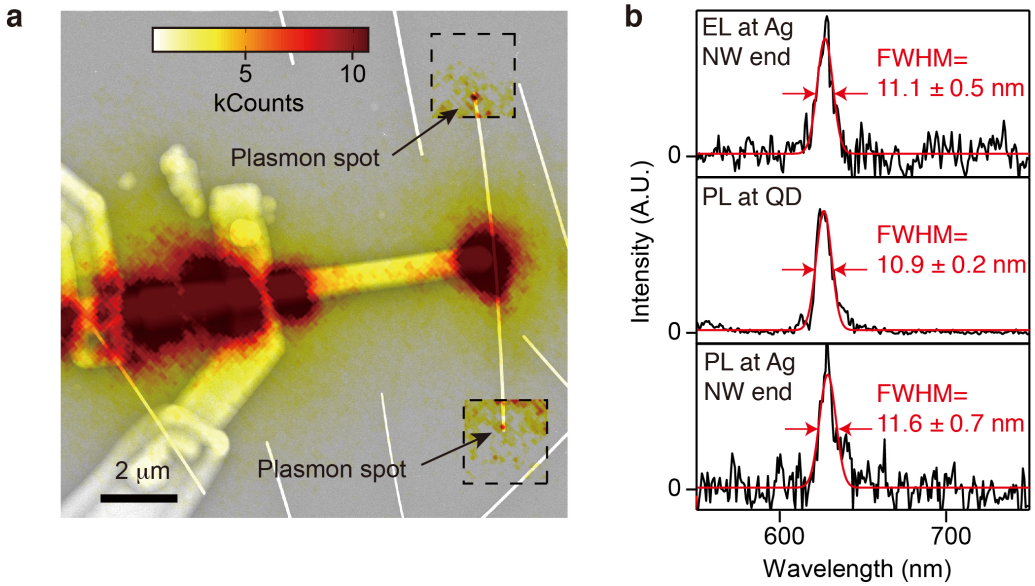

Figure 3.6 | Electro-optical excitation of single surface plasmons polaritons (a) Electroluminescence image of a typical device, recorded with a red color filter. The image is overlaid on an SEM image of the device. Signal around the plasmon out-coupling spots is enhanced by 10 times (enclosed by the dashed rectangles). **(b)** Emission spectra of (top panel) the electro-optically driven SPP from a typical device, (center panel) the quantum dot located at the T-shaped junction and (bottom panel) the surface plasmon when the quantum dot is optically excited by laser. Red lines are their Gaussian fits.

The count rates from the plasmon spots at the end of the nanowire are sufficiently small that it is difficult to obtain a photon auto-correlation measurement from the plasmon spot itself. However, confirmation of the on-chip generation of single plasmons can be obtained by analyzing the plasmon spot spectra. The electro-optically driven single SPPs have a narrow bandwidth defined by their CdSe QD source. A typical SPP out-coupling spot spectrum is shown in the top panel of Figure 3.6b. The spectrum appears as a symmetric peak around 627 nm, with a FWHM linewidth of 11.1 ± 0.5 nm. It clearly resembles the fluorescence spectrum of the quantum dot located at the T-shaped junction, which has a FWHM linewidth of 10.9 ± 0.2 nm (Fig. 3.6b, center panel). The spectral width is much narrower than the ensemble fluorescence spectrum shown in Figure 3.4 (with FWHM ~45 nm) and is mostly inhomogeneously broadened by the quantum dot's spectral diffusion.[103,104] Note that the wavelength of emission has blue-shifted further from Fig. 3.4 because the device is at T~10 K. When the quantum dot at the T-shaped junction is optically excited with a laser and far-field optics, the spectrum of the plasmon out-coupling (bottom panel of Fig. 3.6b) is nearly identical, with an FWHM width of 11.6 ± 0.7 nm. This indeed confirms the CdSe QD can be electrically pumped on chip, to create an integrated single plasmon source.

3.7 Outlook

To the best of our knowledge, the device studied here represents the first demonstration of integrated electro-optical excitation of single surface plasmon polaritons. In the device, incoherent blue photons emitted from an on-chip nanowire LED are converted to single photons at lower frequency through the excitation-emission of a

colloidal quantum dot. The colloidal quantum dot emits into single surface plasmon polaritons, thus greatly enhancing the single photon collection efficiency. The wide spectral range covered by various types of colloidal quantum dots can easily tune the operational frequency of the device from visible to the NIR. This proof-of-principle demonstration can be improved in many ways. First, the NW-based LEDs used in our devices have a relatively low quantum yield, which is due to defects formed during the growth process. A state-of-the-art InGaN/GaN multi-quantum well LED, however, can achieve external quantum efficiency around 50% by strict control of growth conditions and defect levels.[107,108] Incorporation of such an LED would increase the excitation rate of the quantum emitter by orders of magnitude. Second, an emitter with a larger optical absorption cross section will lead to higher efficiency single photon generation. Promising candidates include NV centers in diamond and polycyclic aromatic hydrocarbons, for which the absorption cross- section approaches $\lambda^2/2$ under radiative broadening.[86,109] This can be accomplished by constructing a cavity around the emitter to greatly enhance the Purcell factor to increase the emission rate.[24,110-112] Similarly, a significantly thinner NW can be used to increase the emission rate,[22] and a near-field detector,[89,90] similar to that demonstrated in the next chapter, could improve the single plasmon collection rate.

Chapter 4

Near-field detection of NV centers in diamond waveguides using GaAs APDs

4.1 Overview

As discussed in Section 1.4, diamond's wide bandgap, rigid lattice, and small lattice constant make it difficult to build a photodetector directly out of diamond suitable for detection of color center fluorescence.[54] A better approach for detection of NV centers emission is to combine diamond waveguides containing NVs with a complimentary photodetector material. In this chapter we demonstrate the detection of single NVs using

diamond waveguides transferred onto laterally-defined avalanche photodiodes (APDs) machined from bulk GaAs.

4.2 Requirements for On-Chip Detection of NV Centers

There are three general requirements in order to perform near-field detection of single NV centers. First, the photodetector needs to have significant optical absorption in the range of NV center emission (600-800 nm, for NV^-). Second, the photodetector needs to generate sufficiently high gain to achieve measureable signal for detection of NV centers. Third, is a strongly attenuating blocking layer is likely needed to protect these sensitive detectors from even a small amount of stray pump laser light. The difference in optical power between that emitted by a single NV and the pump beam near NV saturation is ~9 orders of magnitude. One of the benefits of far-field detection of photons is that it is easy to insert optical filters to remove unwanted laser pump light. However, for a near-field detector a spectral filter might be difficult to implement, and therefore it is likely a good blocking layer is needed.

4.3 Possible Integrated Technologies for NV Center Detection

There are few different methods for developing high gain photodetectors on chip with absorption at visible wavelengths. The two broad categories are superconducting detectors and avalanche photodiodes (APDs).

Superconducting photodetectors come in several varieties including transition edge sensors[113], and nanowire detectors.[90,114,115] Superconducting transition edge sensors (TESs) offer high bandwidth, high quantum efficiency over a large spectral range, and

can distinguish photon number and energy. Superconducting nanowire single photon detectors (SNSPDs) do not offer the photon number and energy resolution inherent in the TESs but are also very fast with a large spectral range. Both of these types of detectors are generally operated at cryogenic temperatures well below the critical temperature of the superconductors used to optimize performance. However, TESs are often operated at $T<2$ K, which limits the experimental setups into which they can be integrated.

The physics of avalanche photodiodes (APDs) have been under investigation for more than 50 years.[116] They are composed of carefully doped semiconductors that have large electric fields applied across them. The specific doping schemes of various APDs differ,[117,118] but for illustration consider a normal *p-i-n* diode that is reverse biased in dark. As the reverse bias is increased, the applied electric field will be predominantly in the undoped/lightly-doped intrinsic region. If the electric field across the intrinsic region is large enough, one of two breakdown phenomena will occur. If a thermally generated electron-hole pair is generated in the intrinsic region, it will immediately be separated into electrons and holes by the large applied electric field. If the mean free path in the intrinsic region is large enough, those carriers can have enough kinetic energy that if they collide with the lattice an impact ionization event can occur. These collisions can generate more electrons and holes, which in turn, can generate yet more carriers, and so on. A different breakdown process can occur if the large electric field mediates band-to-band Zener tunneling.[82] The probability of the tunneling event (Θ) scales as $\Theta \propto \exp(-E_g^{3/2})$, where E_g is the bandgap of the semiconductor. These two processes have opposite temperature dependences.[119] As the temperature is reduced, the mean-free path of carriers in the intrinsic region should increase. Therefore carriers can build up

more kinetic energy before a collision and impact ionization becomes more favorable. On the other hand, as the temperature of a typical semiconductor is reduced the bandgap increases, thereby decreasing the tunneling probability. It is possible to distinguish between these two breakdown mechanisms for a diode by monitoring breakdown voltage (V_{BD}) as a function of temperature (T): if breakdown shifts to smaller $|V_{BD}|$ at lower T it is an avalanche process, if it shifts to larger $|V_{BD}|$ at lower T it is a Zener-tunneling dominated process.

It is now easy to understand how an APD generates large gain for an absorbed photon. If there is sufficient electric field, when a photon is absorbed the photogenerated carriers will start the avalanche process. This can occur in two different voltage regimes: below the dark breakdown voltage (what we will refer to as an analog APD measurement) and above it (a Geiger-mode measurement). When performing a measurement below the dark breakdown there generally isn't a large enough electric field to create a full current cascade, but there is analog current amplification from the impact ionization process. Performing photodetection with an APD above the dark breakdown voltage may seem counterintuitive, but the dark breakdown voltage is of a statistical nature.[120] The dark breakdown voltage is the applied bias where there is a large probability that a single carrier in the intrinsic region will lead to breakdown. Therefore, if the voltage is swept quickly past the breakdown voltage there is a brief time window before a dark breakdown event (dark count) occurs. Therefore, if absorption of a single photon can occur in that time window it can be sufficient to cause a huge current cascade. External circuitry can be added to quench the runaway current, and at the same time the voltage can be swept quickly back below breakdown and back past it again, ready for the

next photon.[121] As such, in this type of Geiger-mode measurement the gain is a less well-defined quantity. It is no longer strictly determined by the bias or the intrinsic region width, but also the amount of time the current cascade is allowed to proceed before it is quenched.

APDs operating in Geiger-mode can be used for single photon counting and are widely available as standalone detectors. A typical chip used in a commercial detector is bonded to a thermoelectric cooler to reduce the dark count rate, but the temperature is usually at tens of degrees Celsius below room temperature instead of liquid helium-type temperatures for superconducting detectors. Furthermore, depending on the specific application, the count rates for NVs collected in the near field can be sufficiently high during NV detection that a high dark count rate might be acceptable, thus allowing room temperature device operation. It should be noted that the reset time of avalanche photodiodes is generally slower than superconducting detectors, and the overall switching speed of the avalanche process and probabilistic nature of the photon detection causes more timing jitter. The selection of which near-field detector to use (superconducting vs. APD) depends entirely on the temperature range of interest and timing resolution necessary for the measurements involved. There have been early reports of successful deposition of superconducting NiTiN directly on diamond for eventual measurement of single NV center emission.[122] While these types of superconducting detectors are very promising for single near-field detection, we decided to pursue the goal of NV detection at well-above liquid helium temperatures.

4.4 First Generation Fabrication Scheme Using GaAs Core-Shell *p-i-n* NWs

We decided to pursue the strategy of transferring diamond waveguides onto GaAs APDs. GaAs was selected because it has a much larger gain per unit length than silicon, which is the standard APD material for detection of visible wavelength photons. The tradeoff is that GaAs has greater gain noise than Si.

Nanowire APDs had achieved high gain in a previous experiment using intersecting nanowires of CdS and Si.[123] The method of fabrication of these crossed NW detectors is difficult to scale up. There was an additional experiment beautifully demonstrating the single photon detection from absorption by a InAsP QD embedded in an InP axial *p-i-n* nanowire at T=40 K.[124] The device performance was inspiring, though likely only applicable to quantum emitters in this material system, and not useful for color centers in diamond.

Our initial attempt to generate near-field APDs was pursued with core-shell *p-i-n* GaAs nanowires grown by collaborators via molecular beam epitaxy (MBE).[125,126] The lone dopant used in this growth is silicon, which is incorporated as *p*- or *n*-type depending on specific conditions. To fabricate devices, these nanowires were transferred from the growth subsrate to Si substrates with a 300 nm thick thermal oxide layer. The *n*-type shell is etched away via a non-selective citric acid/hydrogen peroxide mixture in a patterned e-beam resist window. Separate *n*- and *p*-type contacts are deposited separately and the devices are cooled down to liquid nitrogen temperature in our microscope cryostat. A typical device GaAs NW APD device (~60 nm thick intrinsic shell) in shown in Figure 4.1a. Many of these devices did demonstrate avalanche breakdown via a decrease in the magnitude of the breakdown voltage with decreasing temperature (Fig.

4.1b). However, the maximum multiplication values were very modest (M~100) in the best devices, and M~10 was more typical (Fig. 4.1c).

The biggest advantage to this MBE-grown core-shell NW system is that there is an AlGaAs layer deposited around the final GaAs shell that provides epitaxial passivation of the nanowire for reduced surface leakage current. In addition, individual nanowire APDs are wired up on an external insulating substrate, allowing facile electrical isolation of these devices from one another.

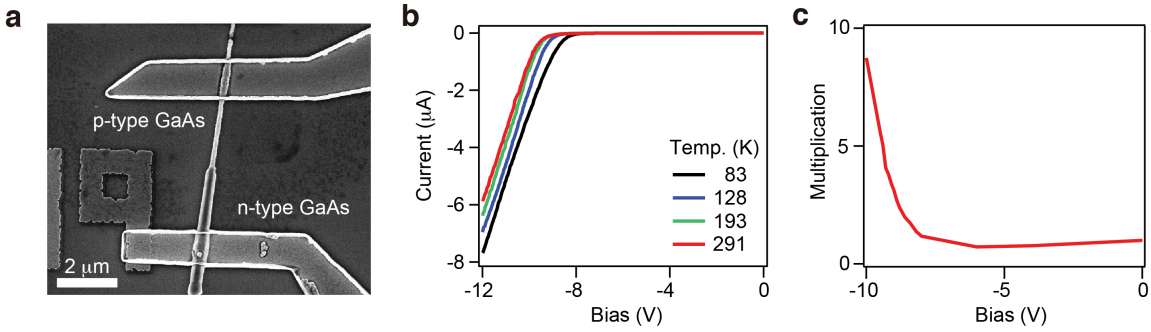

Figure 4.1 | GaAs Nanowire Avalanche Photodiode. (a) SEM image showing a radially etched GaAs core-shell nanowire. **(b)** Temperature dependence of the breakdown process for a typical GaAs core-shell NW APD in dark. **(c)** Modest multiplication of the same device in (b) at T=83 K.

The main disadvantage of this particular core-shell NW system is that the intrinsic shell of this type of nanowire is tapered as part of the growth process. This means that the maximum gain is set by the thinnest portion of this layer, and it is difficult to grow a thick enough intrinsic shell such that the thinnest part can provide enough gain necessary for single NV detection. Also, the core-shell architecture makes it difficult to use optimized *n*-type electrical contacts such as Ni/Ge/Au eutectics because this involves annealing and alloying, which often penetrates into the GaAs layer, and in this case

caused electrical shunting through to the *i*-shell and *p*-core. Unfortunately, well-defined axial *p*-*i*-*n* GaAs nanowires as opposed to core-shell geometries are difficult to generate in this doping scheme because of the different temperature ranges involved in using Si as an ambipolar dopant.

4.5 Improved Top-Down Fabrication Scheme

The limitations of the GaAs NW APDs eventually led to the development of a platform of lateral ion implantation in bulk GaAs to generate larger gain detectors. The improved fabrication scheme to detect single NVs in a diamond waveguide using on-chip detectors is shown in Figure 4.2a. The fabrication of these fully prepared detectors involves many steps, the details of which are delineated in Appendix A.II.3. The starting material for these integrated APDs is bulk semi-insulating GaAs. High gain APDs often have complicated doping profiles, but in this experiment we employ a simple lateral *p*-*i*-*n* design to ensure good alignment of the successive masking steps to define the different doping regions. Specifically these selectively doped regions are generated with electron beam lithography and subsequent reactive ion etching of a thick silicon nitride mask. A deliberate separation of 2-4 μm is designed between the *p*- and *n*-regions, and this is the nominal *i*-region width of the detector. The Be (*p*-type) and Si (*n*-type) implantation is performed at energies of 20 and 75 keV, respectively, corresponding to a nominal depth of 80 nm below the surface. After both implantation steps the device is capped with silicon nitride and annealed at 850°C to remove lattice damage from the implantation and activate the dopants. The silicon nitride capping layer is used to prevent the diffusion of As from the crystal.[127] As a result of this annealing, as well as straggle during the

implantation process, the actual *i*-region width is undoubtedly different from the designed width. After annealing cap removal, *p*- and *n*-type contacts are deposited using standard fabrication techniques with subsequent alloying to reduce contact resistance.

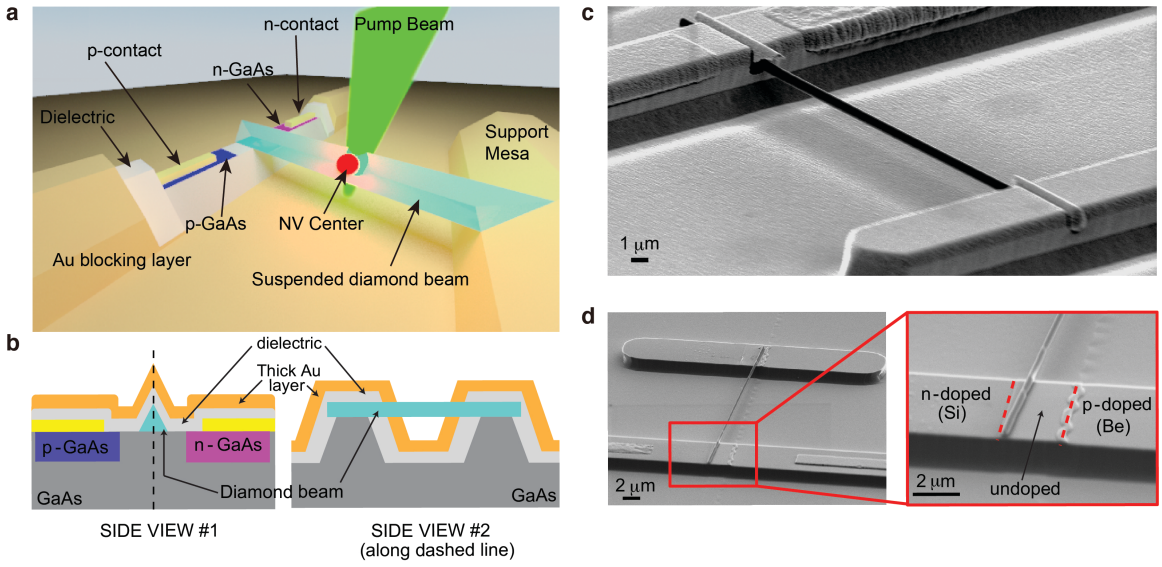

Figure 4.2 | Top-Down Fabrication of GaAs APD/Diamond Device. (a) Schematic diagram of a device measurement with the dielectric/gold blocking layer "peeled back" from the detector to show the diamond beam aligned to the undoped region and spanned by the *p*- and *n*-implanted regions and their respective contacts. **(b)** Cartoon slices through the device to show cross-sections of device with blocking layers. **(c)** SEM image of a complete device including blocking layer. **(d)** SEM images of a device without blocking layers.

To elevate the diamond waveguide above the highly absorptive bulk GaAs (in regions away from the detector), rectangular mesas are defined using electron beam lithography and wet etched to a depth of a few μm below that of the detector and support mesa. To minimize the leakage current at the oxidized surface of GaAs, the surface is chemically stripped of oxides and passivated using ammonium sulfide in isopropyl alcohol. The sulfur atoms temporarily prevent the oxidation of the surface[128,129] until an inorganic passivation layer (silicon nitride or alumina) is deposited on top to permanently cap the

surface. The detectors are typically ~5 μm in width, which according to FDTD simulations is sufficient to absorb all photons into high refractive index GaAs even with the inorganic passivation layer.

The diamond beams are fabricated from type IIA CVD-grown substrates from Element6 via a two-step reactive ion etching process using a Faraday cage[51] as described in Section 1.4, and subsequently annealed.[52] The resulting diamond substrate has large arrays of suspended diamond waveguides typically 30 to 50 μm long and 200-350 nm in diameter. A typical diamond beam fabricated using this process has fewer than 5 NV centers in it.

The diamond beams are extremely robust, but they have deliberate notches etched near the anchors to facilitate controlled breaking. The waveguides are removed from the diamond substrate and placed on the GaAs detectors using a pair of 3-axis closed-loop piezoelectric nano-manipulators with sharp tungsten tips. The large trench generated between the detector and support mesa is useful for the alignment of the diamond beam along the intrinsic region, as it allows the waveguide to be accurately positioned by lifting up the beam from underneath instead of dragging it along the surface of the detector, thereby minimizing damage to both the beam and detector. It is important to note that while the transfer process of the diamond beams in this manner is slow and serial in nature, it is possible to envision a flip-chip process by which the diamond waveguides are transferred accurately *en masse,* as the transparent diamond substrate can be aligned to marks on the detector chip and pressed down to break the waveguides in unison.

After the diamond beams are transferred onto the chip, a thick (200-300 nm) conformal dielectric layer is deposited on the GaAs substrate via alumina atomic layer deposition. This purpose of this dielectric layer is two-fold. First, it electrically insulates the detector and its contacts from the metal blocking layer that will be deposited in the subsequent step. Second, it provides a spacer layer to prevent the metal blocking layer from being in direct contact with the diamond waveuide, which would cause deleterious absorption of photons before they can reach the detector.

Even though the APD has been defined via ion implantation, the bulk GaAs in the bottom of the trench can absorb the laser pump light and the large voltages applied across the detector can allow some of these photogenerated carriers to be collected at the detector. Therefore everything on the chip other than the waveguide itself needs to be covered with a thick metal blocking layer. The most challenging part of the fabrication scheme is selectively removing the metal blocking layer from the diamond waveguide but not the bottom of the trench.

The first step toward producing the blocking layer is performing a thick and relatively conformal gold deposition using DC sputtering. A multi-layer electron beam resist stack is then used to create a mask only for the bottom of the trench but not the waveguide. When the resist is removed from the diamond beam only, successive gold wet etching and dilute hydrofluoric acid etching are used to remove the Au and alumina layers, respectively. This wet etch compatibility, along with the high extinction value of visible light, is why Au is chosen for the metal blocking layer material. A similar additional step is performed to remove the alumina and gold from the wirebonding pads for the GaAs detectors.

4.6 GaAs APD Characterization in Dark

It is important to characterize the GaAs detector without the diamond waveguide and blocking layer to see if it is performing properly. In Figure 4.3a, the current magnitude is plotted logarithmically as function of the applied bias for a nominally 3.7 μm wide intrinsic region device at room temperature in dark. At forward bias, the device is extremely conductive and has a turn-on voltage near 0.7 V, and at reverse bias there is a gradual leakage current and then a sharp breakdown at around -86 V.

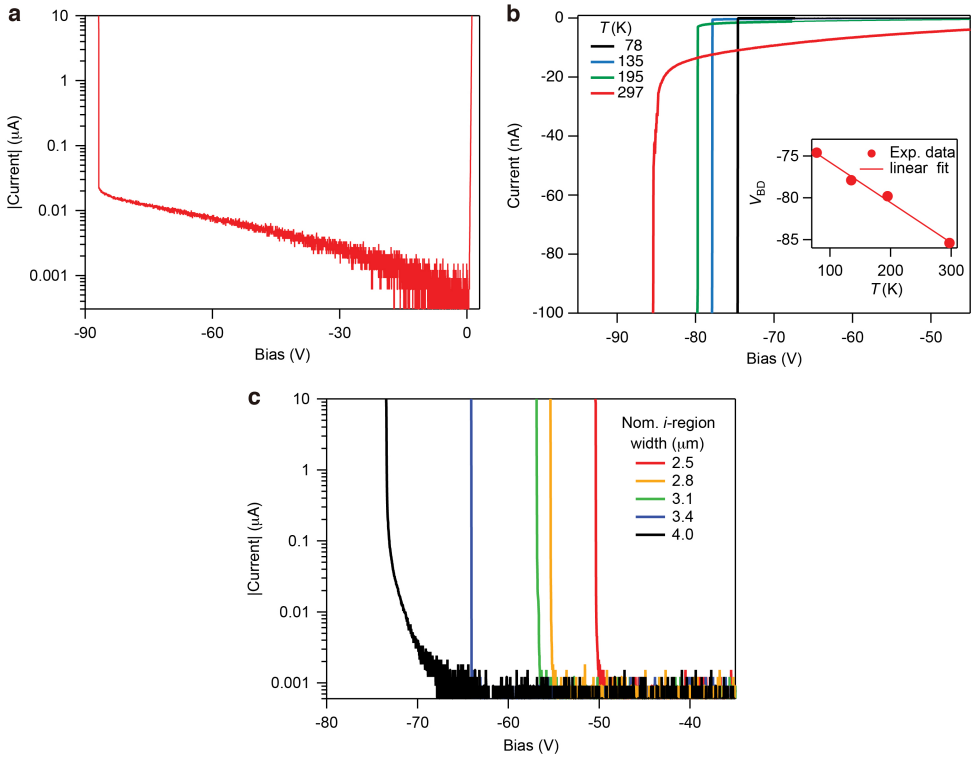

Figure 4.3 | *I-V* curves for laterally-implanted GaAs APDs in dark. (a) Absolute value of the current versus applied voltage for a laterally implanted GaAs APD with a nominal 3.7 μm wide intrinsic region at room temperature. **(b)** Temperature dependence of the breakdown process for the device in (a) in dark. Inset: Breakdown voltage (V_{BD}) as a function of temperature showing a linear fit with a slope of -48 ± 3 mV/K. **(c)** The current magnitude as a function of nominal *i*-region width in reverse bias, for devices from a different chip than (a) and (b).

To investigate this breakdown process and confirm that it is in fact an avalanche breakdown process, current-voltage curves are collected as a function of temperature (Fig. 4.3b). There is an obvious reduction in the magnitude of the breakdown voltage as the sample is cooled with liquid nitrogen. This confirms that the breakdown is an avalanche process as discussed above. The breakdown voltage as a function of temperature is roughly linear and has a decrease in $|V_{BD}|$ of 48 mV/K. While the temperature coefficient of breakdown is dependent on the actual intrinsic region width, this appears to be in the correct range for thin film APDs in GaAs.[130,131]

For every chip there were six different nominal *i*-region widths (2.5, 2.8, …, 4.0 μm). The reason for this intentional sweep is that if the intrinsic region is too short the gain is too low for NV center detection, but on the other hand, the dominant resistance of the device is set by this width and the output current can be limited. The breakdown behavior at T=78 K is shown in Figure 4.3c for five different *i*-widths on a typical chip. There is a monotonic decrease in the $|V_{BD}|$ as a function of the nominal *i*-region width. However, it should be noted that the exact value of V_{BD} for a given width varies by 30% from chip-to-chip depending on the fabrication. Experientially, it appears as though the sulfur passivation and subsequent dielectric deposition step has the largest influence on $V_{BD.}$ It is likely that surface current leakage (as well as unintentional doping from multiple processing steps) can change the actual electric field profile across the *i*-region. Regardless of the exact field profiles, these GaAs devices have confirmed avalanche breakdown, and the next step is determining the maximum gain.

4.7 Gain Characterization for Laterally-Implanted GaAs APDs

Due to limitations in the wiring of the microscope cryostat used in these experiments, fast sweeps of the applied bias above the breakdown voltage (Geiger-mode operation) are difficult without significant signal distortion. As such, all experiments operate below dark breakdown. In this sub-breakdown voltage regime, the multiplication as a function of bias is calculated by:

$$M(V) = \frac{I_{\mathrm{L}}(V) - I_{\mathrm{L}}(0)}{I_{\mathrm{D}}(V) - I_{\mathrm{D}}(0)}$$

where I_{L} is the photocurrent and I_{D} is the dark current. In order to measure the gain for a device it is first necessary to cool down and perform scanning photocurrent imaging. The laser spot is fixed on the intrinsic region while the voltage is swept in reverse bias with and without the laser on. The biggest challenge to accurately determining M is to carefully measure I_{L} and I_{D} at zero bias and take into account current amplifier offsets and hysteresis from stray capacitance. An example gain curve is shown in Figure 4.4a. The highest multiplication in the best devices is ~10^5. The reflection and photocurrent images for the same device at -50 V are shown in Figure 4.4b-c. It is important to note that this photocurrent image was generated by mechanically chopping the laser and using a lock-in amplifier at the chopping frequency, and any DC component to the current signal is filtered out.

The maximum gain value demonstrated of ~10^5 means that for an analog current measurement of an NV center emitting 1 Mcps into a near-field detector, the measured photocurrent current output would be ~10-20 nA assuming unity absorption and impact ionization efficiency. This is a reasonable current level for high signal-to-noise detection.

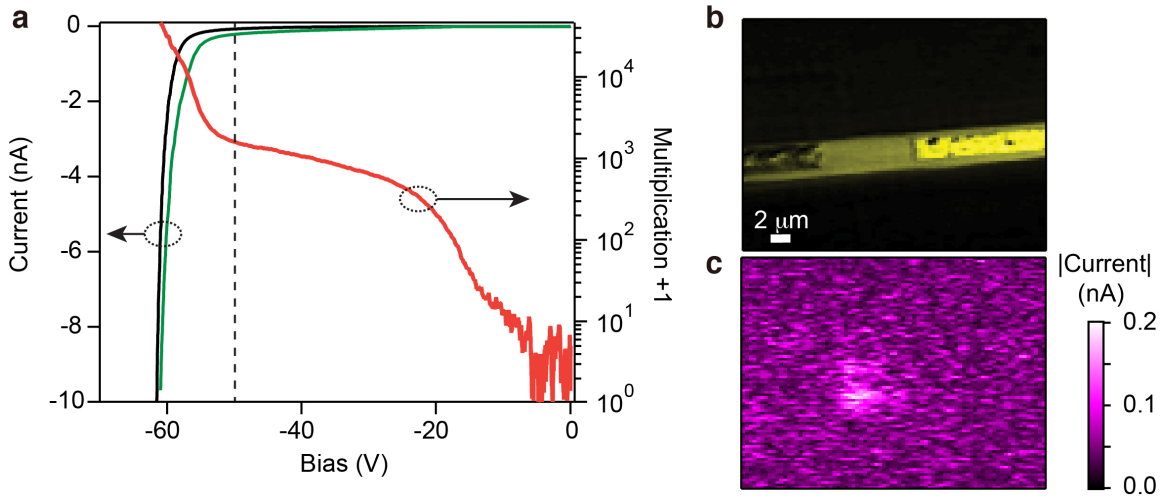

Figure 4.4 | Avalanche gain for a GaAs APD at *T*=78 K. (a) Left axis: dark (black) and light (green) current as a function of reverse bias. The light curve is collected for a 532 nm laser spot of ~100 fW in the intrinsic region of the laterally implanted APD with a nominal width of 3.4 μm at *T*=78 K. Right axis: the red curve shows the multiplication gain of the detector as a function of bias. **(b)** Confocal reflection image of the detector in (a) where the electrodes are visible on either side of the intrinsic region. **(c)** Scanning photocurrent image from the detector shown in (a)-(b) taken at a reverse bias of -50 V, which corresponds to the dashed vertical line in (a).

4.8 Dim Red Laser Coupling to a Diamond Nanobeam

After demonstrating the gain using a top-down laser illumination onto the detector, a more realistic demonstration of NV detection was needed. Diamond beams were transferred onto detectors and support mesas, similar to the SEM images in Figure 4.2c. The diamond beam in this case was engineered with deliberate notches towards the ends, these notches are visible via SEM in the right panel of Figure 4.2d. Without adding the blocking layers, a dim red laser was scanned over the diamond beam to see if the notch position would be apparent via in-coupling to the waveguide. In order to simulate an NV emitting at 1 Mcps, the laser power was attenuated to be 20 Mcps with the assumption that approximately 5% of the photons would couple in and be guided to the APD. As

shown in Figure 4.5b-c, the deliberate notch in the reflection image corresponds exactly to the peak in photocurrent. Again it is important to note that the photocurrent is collected by mechanically chopping the laser input and using a lock-in amplifier for AC current detection.

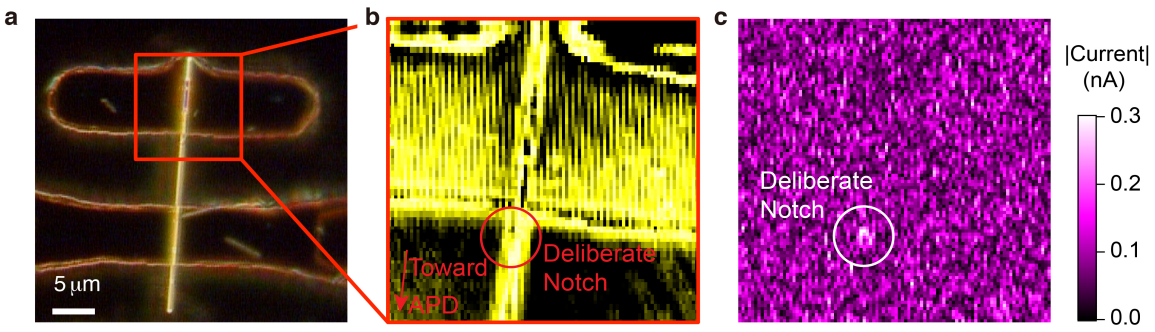

Figure 4.5 | Detection of a simulated NV center at 78 K. (a) A dark field optical image of a diamond nanobeam suspended between a GaAs APD and support mesa without any blocking layers. The diamond beam has deliberate notches along it from the angled reactive ion etching. **(b)** Zoomed-in confocal image reflection image on the deliberate notch near the support mesa. **(c)** Scanning photocurrent image collected using a dim red laser with an estimated input photon flux to the detector of 1 Mcps. The device is biased to -57 V and the bright spot is coincident with the notch in the beam.

4.9 Detection of a Single NV in a Diamond Waveguide

Detection of a simulated NV using a highly attenuated red laser is exciting, but there is no competition with background signal from an intense pump beam, as in the case of pumping an NV to saturation with a 532 nm laser (typically a few 100 μW). The blocking layer scheme shown in Figure 4.2a is essential for detection of a single NV. One of the main challenges is optimizing the time of the Au wet etch to strip the blocking layer from the diamond waveguide. There is a substantial lateral etch rate for Au along the diamond waveguide, and if there is excessive Au near the diamond beam which can scatter in stray light. In contrast, if the Au is etched too much, the detector can be directly exposed to the

pump laser. If the wet etch step is optimized, it is then possible to measure an NV center in a diamond waveguide (Fig. 4.6).

The first step is to find NV centers using a conventional Si SPAD (single photon avalanche detector) in a suspended diamond waveguide. In Figure 4.6b there are four bright spots when looking at the fluorescence along the beam (appropriate filters are in the beam path to block pump light, see Figure A.3). At least the two left-most spots are confirmed single NV centers from autocorrelation measurements showing coincidence dips at $\tau=0$, indicating they are single photon sources.

The NV highlighted in the red/white circle in Figure 4.6b-c is apparent in the scanning photocurrent image with a current magnitude of about ~10 nA, when the device is biased to -60V. The neighboring NV to the left is brighter via far-field collection, but does not show up strongly in the photocurrent measurement. This is likely caused because the NV orientations are different, and NVs with dipole emission along the beam direction can couple strongly the pump laser but do not couple strongly to the waveguide mode inside the diamond.

It is important to note that unlike the scanning measurements demonstrated in Figures 4.4c and 4.5c, this photocurrent measurement wasn't performed using a mechanically-chopped pump laser and lock-in amplifier. Rather, the output of the device was sent to a DC current pre-amplifier. In the previous control experiments, the primary noise source was from current drift from the detector. For this measurement with an intense pump laser, the largest source of unwanted signal is the scattered laser light that can still couple into the detectors despite the blocking layer. A clear example of device features that couple in stray light can be seen along the left side of photocurrent image in Figure 4.6c.

This photocurrent feature arises from the slope of the support mesa created during the wet etch (as can be seen most clearly on the sides of the support mesa in the reflection image), but this feature is not visible in the far-field confocal fluorescence image (Fig. 4.6b). Furthermore, the mechanical chopping of the laser caused issues for the single photon-collection channel in Figure 4.6b. Therefore, performing an AC current lock-in measurement wasn't beneficial as in the other situations.

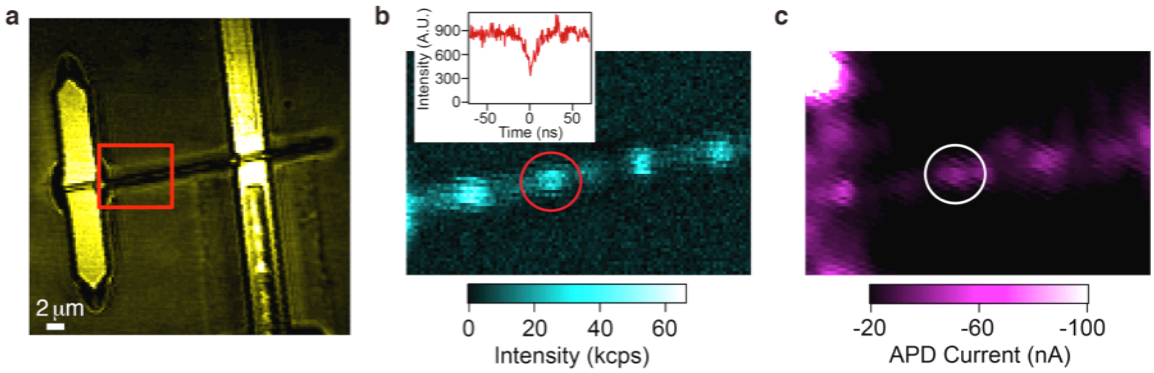

Figure 4.6 | Mapping of NV centers in a diamond beam at 78 K. (a) Confocal reflection image of a diamond beam suspended between support mesa (left) and detector (right). **(b)** Confocal fluorescence image corresponding to the red rectangle in (a). Inset: A photon auto-correlation histogram showing that the fluorescence spot in the red circle is a single NV center. The 532 nm laser pump power is ~120 μW. **(c)** Scanning photocurrent image using GaAs near-field detector of the same portion of the diamond beam as in (b). The 3.7 μm *i*-region width device is biased to -60 V and the bright spot highlighted in the white circle is co-located with the single NV center in (b).

The result of using a DC current pre-amplifier is a large DC current as seen in Figure 4.6c. This is in part because the detector is in large reverse bias and very close to the light breakdown curve. Also, there is a large offset from the background light that is detected through the Au blocking layer, which was only ~200 nm for this particular device. The co-location of a confirmed NV center and a bright photocurrent spot is a great

demonstration of these near-field GaAs detectors; however, much work remains to definitively confirm that these measurements are truly detecting NV center emission.

4.10 Improved detector performance and future work

There is a significant amount of green pump laser light detected using this detector scheme. It is coupling into the detector by one of two pathways. First, the blocking layer around the nanowire leading to the detector isn't perfect, and these gaps allow light to reach the detector. There may be strategies for how to improve this including nickel ALD for more conformal deposition.[132] Second, the green laser can couple into defects in the diamond beam and get guided to the detector. One possible way to improve this is to employ polymer gratings to create a Bragg mirror with a stop band for green light.[24,133]

For the purposes of confirming that the signal in Figure 4.6c is due to NV emission, it would be valuable if the NV blinked on a slow timescale (< 1 Hz). However, one of the primary reasons that NV centers are appealing in a variety applications, is that the single photon emission in the bulk is generally stable and doesn't suffer from the same blinking and photobleaching of other emitters like colloidal quantum dots. There are experiments that demonstrate slow "blinking" of NVs by moving to a pump wavelength such as 593 nm where only NV^- is efficiently pumped.[134] Unfortunately, these experiments use laser powers well below saturation (~1 μW) where the output current from an NV center would likely become too small for detection compared to the background.

A particularly useful "knob" for the NV center is optically detected magnetic resonance (ODMR).[135] When microwaves near 2.88 GHz are resonant with the NV^- triplet ground state they cause an appreciable dip in the NV fluorescence intensity. This

could be employed in this near-field detection geometry to confirm a particular photocurrent spot originates from NV center emission. Beyond demonstrating near-field ODMR, which would be an achievement in its own right, the change in brightness could be used to improve signal-to-noise for the mapping of NVs. If an AC current lock-in measurement is performed as the applied microwave signal (at resonance) is chopped at a slow timescale (<1 kHz), only NVs should respond to the microwave pulse signal, and therefore, the background photocurrent from scattered light should be mitigated.

Overall, the results of this experiment show the possibility of using APDs for near-field collection of NV center emission at liquid nitrogen temperatures. It may be possible for the temperature of operation to be increased by modifying the passivation scheme or deliberately growing AlGaAs on the mesa-etched sample after implantation, rather than relying on sulfur passivation.

This type of near-field detection scheme could also be useful for detection of silicon vacancies (SiV) in diamond. SiVs emit in the NIR, but the count rates of these color centers are generally higher than that of NVs and resonant excitation can be employed to greatly reduce the pump power.[136]

Appendix I:

Confocal Microscope Configurations

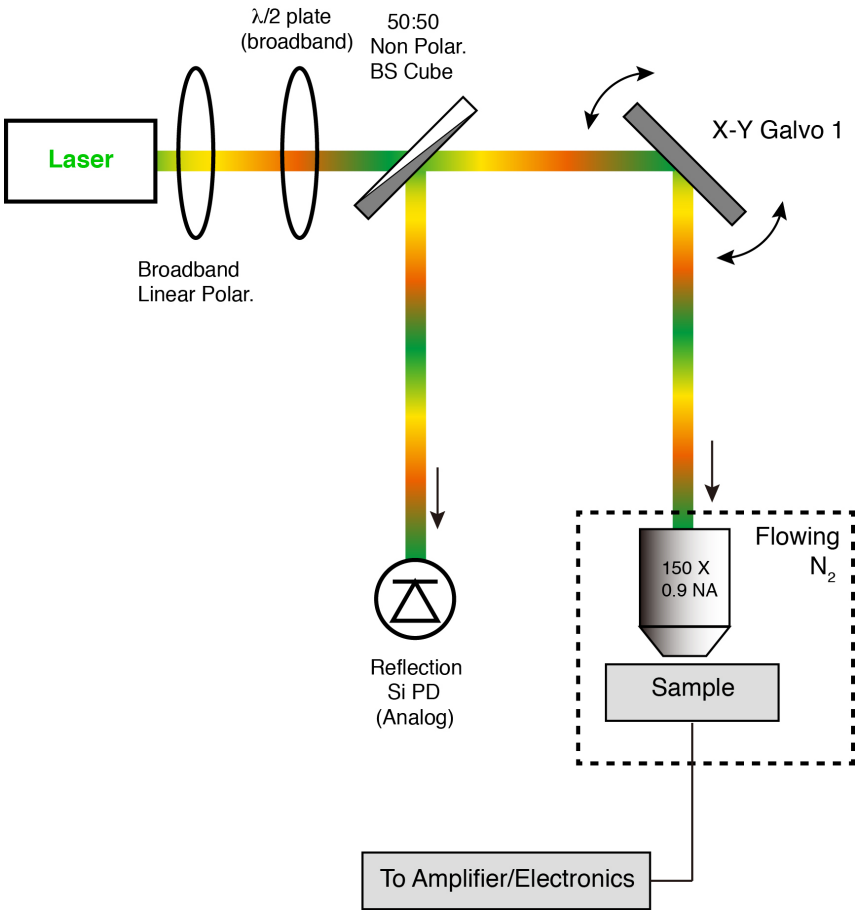

Figure A.1 | Microscope configuration for P3HT/NW experiments. The primary configuration for all measurements in Chapter 2 are shown above. The laser source was either a Compass 315M 532 nm laser or a Koheras SuperK Power supercontinuum source with acousto-optic tunable filter (AOTF) to sweep the wavelength between 470-750 nm. Both lasers were spatially filtered with a pinhole configuration to ensure a diffraction-limited spot. The polarization optics were always rotated to have incident laser polarization along NW axis. The reflection channel was not pin-hole filtered (and not technically confocal, though the NW/P3HT junctions were much thinner than the wavelength, so it likely didn't matter). The telescope lenses for laser scanning—after Galvo 1—were omitted for clarity.

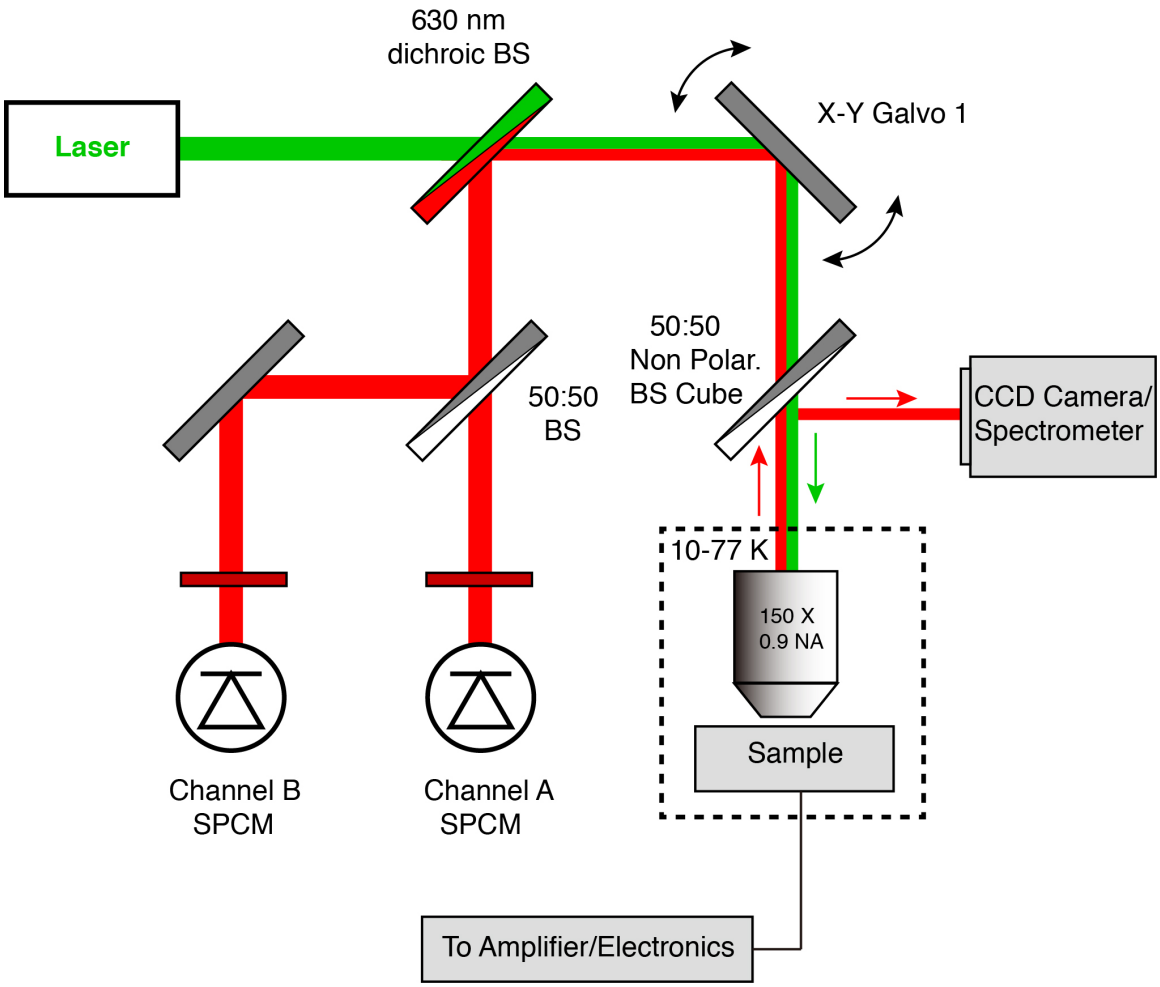

Figure A.2 | Microscope configuration for majority of InGaN/Ag/CdSe experiments. The primary configuration for measurements in Chapter 3 are shown above. The laser source was a Compass 315M 532 nm laser that was spatially filtered with a pinhole configuration to ensure a diffraction-limited spot. The fluorescence channel was (1) split with a 50:50 beamsplitter, (2) confocally collected into two single mode fibers, and (3) and sent to Perkin-Elmer single photon counting modules (SPCM-AQR-14-FC). The autocorrelation measurements were performed with a SPC-630 photon counting card from Becker & Hickl. The telescope lenses for laser scanning—after Galvo 1—were omitted for clarity.

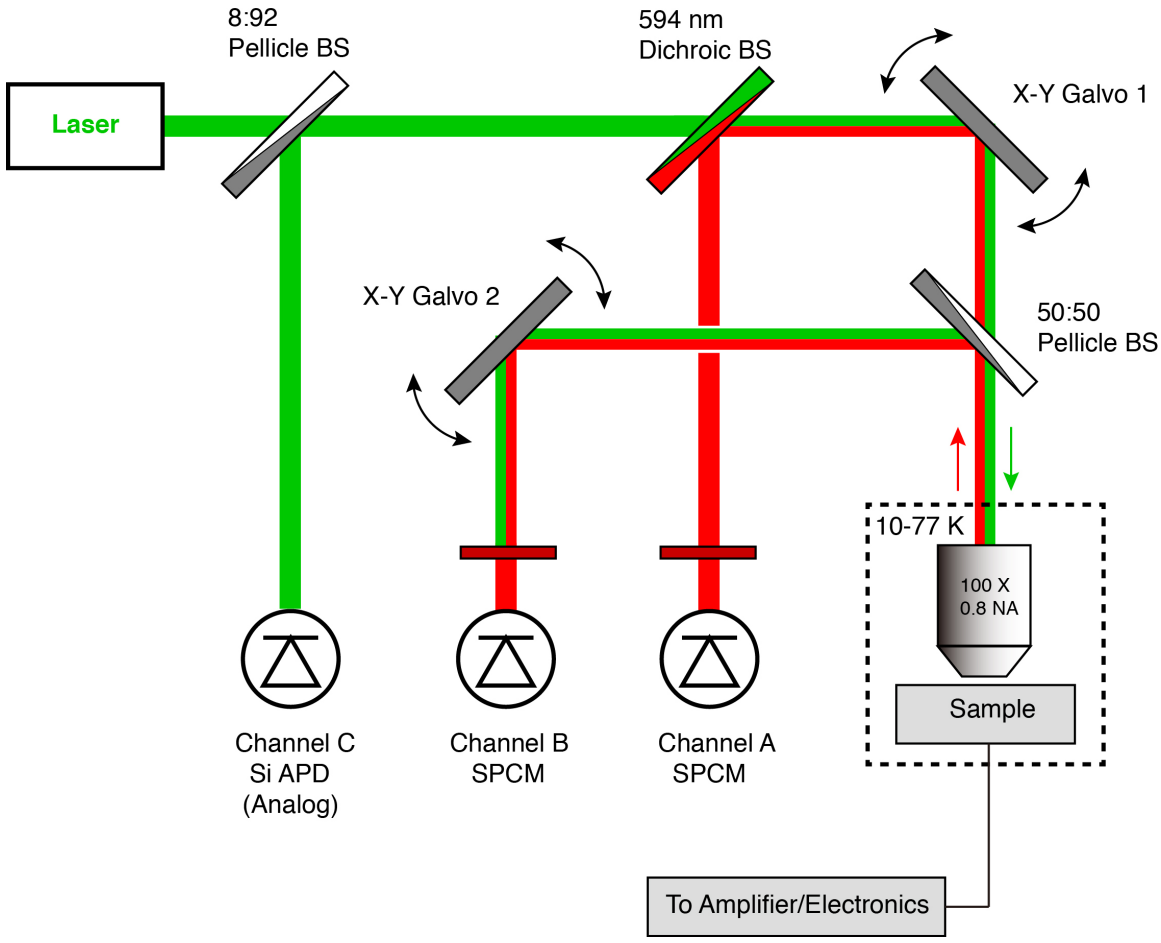

Figure A.3 | Microscope configuration for all diamond/GaAs experiments. The exclusive configuration for all measurements in Chapter 4 are shown above. The laser source was a Compass 315M 532 nm laser that was spatially filtered with single mode optical fiber to ensure a diffraction-limited spot. For Figure 4.5 a 633 nm HeNe laser was inserted after the dichroic BS with its own reflection channel. The two separate fluorescence channels (each on a separate galvo) were (1) split with a 50:50 pellicle beamsplitter, (2) confocally filtered into two single mode fibers, and (3) sent to Perkin-Elmer single photon counting modules (SPCM-AQR-14-FC). The auto-/cross-correlation measurements were performed with a SPC-630 photon counting card from Becker & Hickl. The fluorescence channel fibers could also be connected to a spectrometer/CCD for spectral measurements, as was used for Figure 3.5e and 3.6b. The telescope lenses for laser scanning—after Galvo 1—were omitted for clarity.

Appendix II:

Sample Preparation

A.II.1 Growth/fabrication of NW/P3HT devices

The CdS NWs used in this experiment are synthesized using a solution-liquid-solid method with Bi nanoparticles as catalysts,[67] and are typically 50-100 nm in diameter and 2-4 μm in length. The NWs are suspended in anhydrous hexane and dispersed on silicon chips covered with 300 nm of SiO_2. They are then electrically contacted using conventional electron-beam lithography and metallization with Cr/Au (30 nm/120 nm). A window for the P3HT strip is also defined using electron-beam lithography using MMA and baked at 80°C. This low molecular weight resist and low baking temperature help to ensure the resist dissolves quickly after P3HT spinning. An 8-12 mg/mL solution of regio-regular P3HT (Aldrich) dissolved in anhydrous toluene (Aldrich) at 80°C is spin-coated onto the substrate at 1500 RPM. Lift-off is performed in ethyl acetate to avoid dissolving the P3HT. The polymer strip is typically 40-100 nm thick in the center and has a 400 nm thick frame as determined by atomic force microscopy. If liftoff doesn't work properly, the P3HT can be dissolved in chloroform and gently O_2 plasma cleaned so the NWs can be used reprocessed into new devices.

The CdSe NWs used in this experiment are synthesized using a vapor-liquid-solid method with Au nanoparticles as catalysts and indium as the *n*-type dopant introduced during the growth.[83] The nanowires are typically 50-100 nm in diameter and 5-20 μm in length. The measurement substrate consists of a silicon chip with 300 nm of thermal SiO_2

and 150 nm deep trenches that are etched into the oxide using hydrofluoric acid. Particular care needs to be taken to hard bake the resist before the HF etch step so that there is no delamination of the mask. This leads to wider than intended trenches and the NWs can fall/bend in. The trenches are ~1 μm wide and 20 um long, and have a thin bilayer of Ti/Au (10 nm/40 nm) at the bottom (bringing the total trench depth to 100 nm), which will be used as a contact for the polymer. The NWs are transferred by gently flipping the NW growth substrate on top of the measurement substrate. Both the CdSe NWs and the bottom electrodes in the trench are electrically contacted using conventional electron-beam lithography and metallization with In/Au (15 nm/285 nm) to achieve Ohmic contact. All P3HT steps are the same as listed above for CdS NWs, though care needs to be taken to not elevate the temperature of the CdSe samples, as the melting point of In is very low and the nanowire contacts can reflow.

A.II.2 Growth/fabrication of InGaN/Ag/CdSe devices

The *n*-GaN/*i*-InxGa1-xN/*p*-GaN core/shell/shell nanowires were synthesized by metal-organic chemical vapor deposition (MOCVD), in which the c-axis growth of *n*-GaN cores is first achieved with the nanoparticle-catalysed vapour-liquid-solid (VLS) method. Subsequent radial growth of the shells as reported previously.[97,98] Silicon and magnesium are respectively used as the dopants for *n*-type and *p*-type GaN, respectively. After growth the core-shell NWs are deposited on a 300 nm SiO_2–covered Si substrate via a mechanical chip "flipping" technique. A rectangular etching window is defined at one end of the nanowire by electron beam lithography into thick PMMA. Inside the resist

window the shells are etched away to expose the *n*-GaN core using inductively coupled plasma reactive ion etching (ICP RIE) as reported previously.[97] The nanowire contacts are subsequently defined by two additional e-beam lithography steps using separate metallization recipes: Ti/Al and Ni/Pd for *n*- and *p*- contacts, respectively, via thermal evaporation and annealed at 500°C in forming gas. The yield for successful contact to the *n*-core is rather low (~25%) because the etch depth to the *n*-core is based upon time rather than chemical selectivity, and there is a natural distribution of NW diameters and shell thicknesses.

The silver nanowires were synthesized by the polyol method developed by Sun *et al*.[93] The as-synthesized silver nanowires are cleaned from the ethylene glycol growth solution and dispersed in pure ethanol for deposition. Microfluidic channels (~100 microns wide) in PDMS are used to align the silver nanowires perpendicular to a particular LED.[106] The as-puchased CdSe/ZnS quantum dots are dispersed in decane (Invitrogen, 655 nm), dried under vacuum, and re-dispersed into a 0.5% PMMA solution in chlorobenzene. The solution is spin coated over the device at 5KRPM for 45s. The PMMA layer can be stripped with acetone to remove the quantum dots.

A.II.3 Fabrication of GaAs APDs

We start with 4" bulk GaAs (100) semi-insulating wafers from University Wafer. ZEP 520A e-beam resist is spun at 3KRPM on the sample and baked at 180 C for 5 min. The marker pattern for the devices is written on the sample and it is subsequently etched in an ICP RIE using BCl3/Cl2/Ar chemistry. The sample is then cleaned in Remover PG overnight and 450 nm of PECVD Si_3N_4 (mixed-frequency) is deposited on the sample.

ZEP 520A is again used as the e-beam mask and the windows for the Be implantation are written. The windows are transferred to the Si_3N_4 mask via SF_6/CHF_3 etch chemistry. Care is taken to not over-etch the sample. The sample is sent to Innovion for Be implantation (20 keV and $9.2x10^{12}$ cm^{-2}). After implantation the mask is removed in HF and the Si windows are written/transferred exactly as was done for Be. The Si implantation is done at 75 keV and $1x10^{13}$ cm^{-2}.

After implantation and mask removal, the sample is thoroughly stripped of oxide and put into a RF sputtering chamber with a loadlock to prevent oxide formation. Approximately 30 nm of Si_3N_4 is deposited in an Ar atmosphere. The sample is subsequently annealed at 850°C for 1 min in a rapid thermal annealing (RTA) chamber under nitrogen. The annealing cap layer is stripped off the sample and an EL11/PMMA C2 layer is spun on the wafer to define the *p*-type contacts. Au/Zn/Au (20/5/75 nm) is deposited via thermal evaporation for the *p*-type contact and standard liftoff is performed in acetone. A similar procedure is performed for Ni/Ge/Au/Ni/Au (10/30/20/20/40 nm) is thermally evaporated for the *n*-type contact. The sample is put in a RTA for a 1 minute anneal at 415°C to alloy the contacts.

The sample is then coated at 3KRPM with maN-2403 negative e-beam resist. The mesa pattern is written on the sample and it is developed for 70s in MF-319 developer. This wet etch mask is particularly fickle depending on the age of the resist, and adhesion promoters can be helpful. The mesas are etched in a citric acid/hydrogen peroxide or phosphoric acid/hydrogen peroxide solution. The etch depths are 2-4 μm and then the maN-2403 can be stripped with acetone and oxygen plasma. The sulfur passivation is performed with 10 mL of 40% ammonium sulfide solution mixed with 40 mL of

isopropanol. After dilute HCl and ammonium hydroxide oxide removal steps, the chip is left submerged in clean DI water. It isn't exposed to atmosphere but is transferred to IPA with successive dilutions and then the chip is soaked for 3-5 minutes in the ammonium sulfide/IPA mixture. A sputtering step—similar to that used for the annealing cap layer—is used to encapsulate the sulfur passivation.

The detector itself is now complete, but the diamond beam needs to be transferred using nanomanipulators to position it in the intrinsic region of the detector. After the diamond beams are transferred onto the chip, a 200-300 nm thick layer of ALD is deposited at 150°C. If the fluorescence of the diamond beams is investigated with the ALD layer on it, there will be a huge background signal, however, it can be burned off using extended exposure at high 532 nm laser power (~10 mW). The extent of the background appears to be related to the ALD deposition temperature, but more work needs to be done to confirm this. After the alumina deposition step a 200-400 nm thick layer of gold is DC sputtered on the sample. This is the foundation for the metal mask.

With this gold layer in place, a five-layer electron beam resist stack is spun onto the sample. These layers are thick and therefore baked at 180C for 15 min each. Spun first on the chip is a bilayer of PMMA C7. Then a tri-layer of ZEP 520A is spun on top. ZEP has approximately a 5x higher sensitivity to electron-beam exposure than PMMA. Therefore we can perform electron beam lithography to open up a window in the ZEP but leave the PMMA intact. An isotropic O_2 plasma clean is performed to slowly etch away residual PMMA around the suspended diamond waveguide. After each short etching step the clarity of the diamond beam under the optical microscope reveals if the desired portion of the waveguide is free of resist. The sample is then wet etched in Transene Au etchant,

and dilute HF, to remove the gold and alumina, respectively. Once the diamond waveguide is clear of gold and alumina the resist can easily be solvent stripped again in Remover PG. A similar step is performed on the wirebonding pads before the diamond beam is etched, but care is taken to not completely etch through the alumina. A thin layer (20-30 nm) is left on the sample to prevent the undercut Au mask layer from shorting to the device electrodes but this is thin enough to be punched through during the wirebonding process.

Bibliography

1 You, J. *et al.* A polymer tandem solar cell with 10.6% power conversion efficiency. *Nat. Commun.* **4**, 1446 (2013).

2 Liang, Y. *et al.* For the bright future-bulk heterojunction polymer solar cells with power conversion efficiency of 7.4%. *Adv. Mater.* **22**, E135 (2010).

3 Bennett, C. H. Quantum cryptography using any 2 nonorthogonal states. *Phys. Rev. Lett.* **68**, 3121 (1992).

4 Lukin, M. D. Colloquium: Trapping and manipulating photon states in atomic ensembles. *Rev. Mod. Phys.* **75,** 457 (2003).

5 Lvovsky, A. I. *et al.* Quantum state reconstruction of the single-photon Fock state. *Phys. Rev. Lett.* **87**, 050402 (2001).

6 Lamas-Linares, A., Simon, C., Howell, J. C. & Bouwmeester, D. Experimental quantum cloning of single photons. *Science* **296**, 712 (2002).

7 McNeill, C. R. & Greenham, N. C. Conjugated-Polymer Blends for Optoelectronics. *Adv. Mater.* **21**, 3840 (2009).

8 Heeger, A. J. 25th anniversary article: Bulk heterojunction solar cells: understanding the mechanism of operation. *Adv. Mater.* **26**, 10 (2014).

9 Kroeze, J. E., Savenije, T. J., Vermeulen, M. J. W. & Warman, J. M. Contactless determination of the photoconductivity action spectrum, exciton diffusion length, and charge separation efficiency in polythiophene-sensitized TiO2 bilayers. *J. Phys. Chem. B* **107**, 7696 (2003).

10 Shaw, P. E., Ruseckas, A. & Samuel, I. D. W. Exciton diffusion measurements in poly(3-hexylthiophene). *Adv. Mater.* **20**, 3516 (2008).

11 Mihailetchi, V., Koster, L., Hummelen, J. & Blom, P. Photocurrent Generation in Polymer-Fullerene Bulk Heterojunctions. *Phys. Rev. Lett.* **93**, 216601 (2004).

12 Cowan, S. R., Roy, A. & Heeger, A. J. Recombination in polymer-fullerene bulk heterojunction solar cells. *Phys. Rev. B* **82**, 245207 (2010).

13 Barker, J., Ramsdale, C. & Greenham, N. Modeling the current-voltage characteristics of bilayer polymer photovoltaic devices. *Phys. Rev. B* **67**, 075205 (2003).

14 Park, S. H. *et al.* Bulk heterojunction solar cells with internal quantum efficiency approaching 100%. *Nature Photon.* **3**, 297 (2009).

15 Huynh, W. U., Dittmer, J. J. & Alivisatos, A. P. Hybrid nanorod-polymer solar cells. *Science* **295**, 2425 (2002).

16 Takahara, J., Yamagishi, S., Taki, H., Morimoto, A. & Kobayashi, T. Guiding of a one-dimensional optical beam with nanometer diameter. *Opt. Lett.* **22**, 475 (1997).

17 Zia, R., Selker, M. D., Catrysse, P. B. & Brongersma, M. L. Geometries and materials for subwavelength surface plasmon modes. *J. Opt. Soc. Am. A* **21**, 2442 (2004).

18 Bozhevolnyi, S. I., Volkov, V. S., Devaux, E. & Ebbesen, T. W. Channel Plasmon-Polariton Guiding by Subwavelength Metal Grooves. *Phys. Rev. Lett.* **95**, 046802 (2005).

19 Oulton, R. F., Sorger, V. J., Genov, D. A., Pile, D. F. P. & Zhang, X. A hybrid plasmonic waveguide for subwavelength confinement and long-range propagation. *Nature Photon.* **2**, 496 (2008).

20 Oulton, R. F. *et al.* Plasmon lasers at deep subwavelength scale. *Nature* **461**, 629 (2009).

21 Quinten, M., Leitner, A., Krenn, J. R. & Aussenegg, F. R. Electromagnetic energy transport via linear chains of silver nanoparticles. *Opt. Lett.* **23**, 1331 (1998).

22 Chang, D. E., Sorensen, A. S., Hemmer, P. R. & Lukin, M. D. Quantum optics with surface plasmons. *Phys. Rev. Lett.* **97**, 053002 (2006).

23 Englund, D. *et al.* Controlling the Spontaneous Emission Rate of Single Quantum Dots in a Two-Dimensional Photonic Crystal. *Phys. Rev. Lett.* **95**, 013904 (2005).

24 de Leon, N. P. *et al.* Tailoring light-matter interaction with a nanoscale plasmon resonator. *Phys. Rev. Lett.* **108**, 226803 (2012).

25 Santori, C., Pelton, M., Solomon, G. S., Dale, Y. & Yamamoto, Y. Triggered single photons from a quantum dot. *Phys. Rev. Lett.* **86**, 1502 (2001).

26 Akimov, A. V. *et al.* Generation of single optical plasmons in metallic nanowires coupled to quantum dots. *Nature* **450**, 402 (2007).

27 Yuan, Z. L. *et al.* Electrically driven single-photon source. *Science* **295**, 102 (2002).

28 Heindel, T. *et al.* Electrically driven quantum dot-micropillar single photon source with 34% overall efficiency. *Appl. Phys. Lett.* **96**, 011107 (2010).

29 Bennett, A. J. *et al.* Microcavity single-photon-emitting diode. *Appl. Phys. Lett.* **86**, 181102 (2005).

30 Castelletto, S. *et al.* A silicon carbide room-temperature single-photon source. *Nat. Mater.* **13**, 151 (2014).

31 Morfa, A. J. *et al.* Single-photon emission and quantum characterization of zinc oxide defects. *Nano Lett.* **12**, 949 (2012).

32 Zaitsev, A. M. *Optical Properties of Diamond: A Data Handbook*. (Springer-Verlag, 2001).

33 Gruber, A. *et al.* Scanning confocal optical microscopy and magnetic resonance on single defect centers. *Science* **276**, 2012 (1997).

34 Davies, G. & Hamer, M. F. Optical Studies of the 1.945 eV Vibronic Band in Diamond. *Proc. R. Soc. A* **348**, 285 (1976).

35 Balasubramanian, G. *et al.* Ultralong spin coherence time in isotopically engineered diamond. *Nat. Mater.* **8**, 383 (2009).

36 Yu, S. J., Kang, M. W., Chang, H. C., Chen, K. M. & Yu, Y. C. Bright Fluorescent Nanodiamonds- No Photobleaching and Low Cytotoxicity. *J. Am. Chem. Soc.* **127**, 17604 (2005).

37 Kucsko, G. *et al.* Nanometre-scale thermometry in a living cell. *Nature* **500**, 54 (2013).

38 Maze, J. R. *et al.* Nanoscale magnetic sensing with an individual electronic spin in diamond. *Nature* **455**, 644 (2008).

39 Dolde, F. *et al.* Electric-field sensing using single diamond spins. *Nature Phys.* **7**, 459 (2011).

40 Sushkov, A. O. *et al.* Magnetic Resonance Detection of Individual Proton Spins Using Quantum Reporters. *Phys. Rev. Lett.* **113**, 197601 (2014).

41 Gurudev Dutt, M. V. *et al.* Quantum Register Based on Individual Electronic and Nuclear Spin Qubits in Diamond. *Science* **316**, 1312 (2007).

42 Babinec, T. M. *et al.* A diamond nanowire single-photon source. *Nat. Nanotechnol.* **5**, 195 (2010).

43 Hadden, J. P. *et al.* Strongly enhanced photon collection from diamond defect centers under microfabricated integrated solid immersion lenses. *Appl. Phys. Lett.* **97**, 241901 (2010).

44 Marseglia, L. *et al.* Nanofabricated solid immersion lenses registered to single emitters in diamond. *Appl. Phys. Lett.* **98**, 133107 (2011).

45 Chen, X. W., Gotzinger, S. & Sandoghdar, V. 99% efficiency in collecting photons from a single emitter. *Opt. Lett.* **36**, 3545 (2011).

46 Lee, K. G. *et al.* A planar dielectric antenna for directional single-photon emission and near-unity collection efficiency. *Nature Photon.* **5**, 166 (2011).

47 Riedel, D. *et al.* Low-Loss Broadband Antenna for Efficient Photon Collection from a Coherent Spin in Diamond. *Phys. Rev. Appl.* **2**, 064011 (2014).

48 Shields, B. J., Unterreithmeier, Q. P., de Leon, N. P., Park, H. & Lukin, M. D. Efficient readout of a single spin state in diamond via spin-to-charge conversion. *arXiv:1410.0370v1* (2014).

49 Babinec, T. M., Choy, J. T., Smith, K. J. M., Khan, M. & Lončar, M. Design and focused ion beam fabrication of single crystal diamond nanobeam cavities. *J. Vac. Sci. Tech. B* **29**, 010601 (2011).

50 Hausmann, B. J. M. *et al.* Coupling of NV centers to photonic crystal nanobeams in diamond. *Nano Lett.* **13**, 5791 (2013).

51 Burek, M. J. *et al.* Free-standing mechanical and photonic nanostructures in single-crystal diamond. *Nano Lett.* **12**, 6084 (2012).

52 Chu, Y. *et al.* Coherent optical transitions in implanted nitrogen vacancy centers. *Nano Lett.* **14**, 1982 (2014).

53 Burek, M. J. *et al.* High quality-factor optical nanocavities in bulk single-crystal diamond. *Nat. Commun.* **5**, 5718 (2014).

54 Chen, K. H., Wu, J. Y., Chen, L. C., Juan, C. C. & Hsu, T. in *Proceedings of the Symposium on Wide Bandgap Semiconductors and Devices and the Twenty-Third State-of-the-Art Program on Compound Semiconductors*. (eds F. Ren *et al.*) 55 (The Electrochemical Society, 1995).

55 Mizuochi, N. *et al.* Electrically driven single-photon source at room temperature in diamond. *Nature Photon.* **6**, 299 (2012).

56 Lohrmann, A. *et al.* Diamond based light-emitting diode for visible single-photon emission at room temperature. *Appl. Phys. Lett.* **99**, 251106 (2011).

57 Greenham, N. C., Peng, X. G. & Alivisatos, A. P. Charge separation and transport in conjugated-polymer/semiconductor-nanocrystal composites studied by photoluminescence quenching and photoconductivity. *Phys. Rev. B* **54**, 17628 (1996).

58 Nozik, A. J. Quantum dot solar cells. *Physica E* **14**, 115 (2002).

59 Huynh, W. U. *et al.* Charge transport in hybrid nanorod-polymer composite photovoltaic cells. *Phys. Rev. B* **67**, 115326 (2003).

60 Quist, P. A. C. *et al.* Photogeneration and decay of charge carriers in hybrid bulk heterojunctions of ZnO nanoparticles and conjugated polymers. *J. Phys. Chem. B* **110**, 10315 (2006).

61 Dietmueller, R. *et al.* Light-induced charge transfer in hybrid composites of organic semiconductors and silicon nanocrystals. *Appl. Phys. Lett.* **94**, 113301 (2009).

62 Bi, H. & LaPierre, R. R. A GaAs nanowire/P3HT hybrid photovoltaic device. *Nanotechnology* **20**, 465205 (2009).

63 Gregg, B. A. Excitonic solar cells. *J. Phys. Chem. B* **107**, 4688 (2003).

64 Kim, S. S., Na, S. I., Jo, J., Tae, G. & Kim, D. Y. Efficient Polymer Solar Cells Fabricated by Simple Brush Painting. *Adv. Mater.* **19**, 4410 (2007).

65 Briseno, A. L. *et al.* Oligo- and Polythiophene/ZnO Hybrid Nanowire Solar Cells. *Nano Lett.* **10**, 334 (2010).

66 Ozel, T., Bourret, G. R., Schmucker, A. L., Brown, K. A. & Mirkin, C. A. Hybrid Semiconductor Core-Shell Nanowires with Tunable Plasmonic Nanoantennas. *Adv. Mater.* **25**, 4515 (2013).

67 Ouyang, L., Maher, K. N., Yu, C. L., McCarty, J. & Park, H. Catalyst-assisted solution-liquid-solid synthesis of CdS/CdSe nanorod heterostructures. *J. Am. Chem. Soc.* **129**, 133 (2007).

68 Norrman, K., Gevorgyan, S. A. & Krebs, F. C. Water-induced degradation of polymer solar cells studied by H2(18)O labeling. *ACS Appl. Mater. Inter.* **1**, 102 (2009).

69 Fumagalli, L. *et al.* Al2O3 as gate dielectric for organic transistors: Charge transport phenomena in poly-(3-hexylthiophene) based devices. *Org. Electron.* **9** (2008).

70 Ahn, Y., Dunning, J. & Park, J. Scanning photocurrent imaging and electronic band studies in silicon nanowire field effect transistors. *Nano Lett.* **5**, 1367 (2005).

71 Gu, Y., Romankiewicz, J. P., David, J. K., Lensch, J. L. & Lauhon, L. J. Quantitative measurement of the electron and hole mobility-lifetime products in semiconductor nanowires. *Nano Lett.* **6**, 948 (2006).

72 Scully, S. R. & McGehee, M. D. Effects of optical interference and energy transfer on exciton diffusion length measurements in organic semiconductors. *J. Appl. Phys.* **100**, 034907 (2006).

73 Wang, J. F., Gudiksen, M. S., Duan, X. F., Cui, Y. & Lieber, C. M. Highly polarized photoluminescence and photodetection from single indium phosphide nanowires. *Science* **293**, 1455 (2001).

74 Ninomiya, S. & Adachi, S. Optical properties of wurtzite CdS. *J. Appl. Phys.* **78**, 1183 (1995).

75 Naqvi, K. R., Mork, K. J. & Waldenstrom, S. Reduction of the Fokker-Planck Equation with an Absorbing or Reflecting Boundary to the Diffusion Equation and the Radiation Boundary Condition. *Phys. Rev. Lett.* **49**, 304 (1982).

76 Weber, C., Becker, U., Renner, R., and Klingshirn, C. Measurement of the diffusion-length of carriers and excitons in CdS using laser-induced transient gratings. *Z. Phys. B* **72**, 379 (1988).

77 Diemer, G. & Hoogenstraaten, W. Ambipolar and exciton diffusion in CdS crystals. *J. Phys. Chem. Solids.* **2**, 119 (1957).

78 Basko, D. M. & Conwell, E. M. Hot exciton dissociation in conjugated polymers. *Phys. Rev. B* **66**, 155210 (2002).

79 Hendry, E., Schins, J. M., Candeias, L. P., Siebbeles, L. D. A. & Bonn, M. Efficiency of Exciton and Charge Carrier Photogeneration in a Semiconducting Polymer. *Phys. Rev. Lett.* **92**, 196601 (2004).

80 Dicker, G., de Haas, M. P., Warman, J. M., de Leeuw, D. M. & Siebbeles, L. D. A. The Disperse Charge-Carrier Kinetics in Regioregular Poly(3-hexylthiophene). *J. Phys. Chem. B* **108**, 17818 (2004).

81 Fahrenbruch, A. L. & Bube, R. H. *Fundamentals of solar cells: photovoltaic solar energy conversion*. (Academic Press, 1983).

82 Zener, C. A Theory of the Electrical Breakdown of Solid Dielectrics. *Proc. R. Soc. A* **145**, 523 (1934).

83 He, Z. *et al.* Tuning Electrical and Photoelectrical Properties of CdSe Nanowires via Indium Doping. *Small* **5**, 345 (2009).

84 Ninomiya, S. & Adachi, S. Optical properties of cubic and hexagonal CdSe. *J. Appl. Phys.* **78**, 4681 (1995).

85 Michler, P. *et al.* Quantum correlation among photons from a single quantum dot at room temperature. *Nature* **406**, 968 (2000).

86 Kurtsiefer, C., Mayer, S., Zarda, P. & Weinfurter, H. Stable solid-state source of single photons. *Phys. Rev. Lett.* **85**, 290 (2000).

87 Wang, J. F., Gudiksen, M. S., Duan, X. F., Cui, Y. & Lieber, C. M. Highly polarized photoluminescence and photodetection from single indium phosphide nanowires. *Science* **293**, 1455 (2001).

88 Huang, Y., Duan, X. F. & Lieber, C. M. Nanowires for integrated multicolor nanophotonics. *Small* **1**, 142 (2005).

89 Falk, A. L. *et al.* Near-field electrical detection of optical plasmons and single-plasmon sources. *Nature Phys.* **5** (2009).

90 Heeres, R. W. *et al.* On-chip single plasmon detection. *Nano Lett.* **10**, 661 (2010).

91 Chang, D. E., Sorensen, A. S., Demler, E. A. & Lukin, M. D. A single-photon transistor using nanoscale surface plasmons. *Nature Phys.* **3**, 807 (2007).

92 Murray, C. B., Kagan, C. R. & Bawendi, M. G. Synthesis and characterization of monodisperse nanocrystals and close-packed nanocrystal assemblies. *Annu. Rev. Mater. Sci.* **30**, 545 (2000).

93 Sun, Y. G., Gates, B., Mayers, B. & Xia, Y. N. Crystalline silver nanowires by soft solution processing. *Nano Lett.* **2**, 165 (2002).

94 Ditlbacher, H. *et al.* Silver nanowires as surface plasmon resonators. *Phys. Rev. Lett.* **95**, 257403 (2005).

95 Johnson, P. B. & Christy, R. W. Optical-constants of noble-metals. *Phys. Rev. B* **6**, 4370 (1972).

96 Ejder, E. Refractive Index of GaN. *Phys. Status Solidi A* **6**, 445 (1971).

97 Dong, Y. J., Tian, B. Z., Kempa, T. J. & Lieber, C. M. Coaxial Group III-nitride nanowire photovoltaics. *Nano Lett.* **9**, 2183 (2009).

98 Qian, F. *et al.* Gallium nitride-based nanowire radial heterostructures for nanophotonics. *Nano Lett.* **4**, 1975 (2004).

99 Calleja, E. *et al.* Yellow luminescence and related deep states in undoped GaN. *Phys. Rev. B* **55**, 4689 (1997).

100 Manz, C., Kunzer, M., Obloh, H., Ramakrishnan, A. & Kaufmann, U. $In_xGa_{1-x}N$/GaN band offsets as inferred from the deep, yellow-red emission band in $In_xGa_{1-x}N$. *Appl. Phys. Lett.* **74**, 3993 (1999).

101 Reshchikov, M. A. & Morkoc, H. Luminescence properties of defects in GaN. *J. Appl. Phys.* **97** (2005).

102 Valerini, D. *et al.* Temperature dependence of the photoluminescence properties of colloidal CdSe/ZnS core/shell quantum dots embedded in a polystyrene matrix. *Phys. Rev. B* **71**, 235409 (2005).

103 Empedocles, S. A., Norris, D. J. & Bawendi, M. G. Photoluminescence Spectroscopy of Single CdSe Nanocrystallite Quantum Dots. *Phys. Rev. Lett.* **77**, 3873 (1996).

104 Blanton, S. A., Hines, M. A. & Guyot-Sionnest, P. Photoluminescence wandering in single CdSe nanocrystals. *Appl. Phys. Lett.* **69**, 3905 (1996).

105 Hausmann, D., Becker, J., Wang, S. L. & Gordon, R. G. Rapid vapor deposition of highly conformal silica nanolaminates. *Science* **298**, 402 (2002).

106 Huang, Y., Duan, X., Wei, Q. & Lieber, C. M. Directed Assembly of One-Dimensional Nanostructures into Functional Networks. *Science* **291**, 630 (2001).

107 Kim, K. C. *et al.* Improved electroluminescence on nonpolar m-plane InGaN/GaN quantum wells LEDs. *Phys. Status Solidi RLL* **1**, 125 (2007).

108 Zhao, Y. J. *et al.* High-Power Blue-Violet Semipolar (2021) InGaN/GaN Light-Emitting Diodes with Low Efficiency Droop at 200 A/cm^2. *Appl. Phys. Express* **4**, 082104 (2011).

109 Rezus, Y. L. A. *et al.* Single-Photon Spectroscopy of a Single Molecule. *Phys. Rev. Lett.* **108**, 093601 (2012).

110 Min, B. K. *et al.* High-Q surface-plasmon-polariton whispering-gallery microcavity. *Nature* **457**, 455 (2009).

111 Choy, J. T. *et al.* Enhanced single-photon emission from a diamond-silver aperture. *Nature Photon.* **5**, 738 (2011).

112 de Leon, N. P. *et al.* Tailoring light-matter interaction with a nanoscale plasmon resonator. *Phys Rev Lett* **108** (2012).

113 Cabrera, B. *et al.* Detection of single infrared, optical, and ultraviolet photons using superconducting transition edge sensors. *Appl. Phys. Lett.* **73**, 735 (1998).

114 Gol'tsman, G. *et al.* Fabrication and Properties of an Ultrafast NbN Hot-Electron Single-Photon Detector. *IEEE Trans. Appl. Supercond.* **11**, 574 (2001).

115 Gol'tsman, G. *et al.* Picosecond superconducting single-photon optical detector. *Appl. Phys. Lett.* **79**, 705 (2001).

116 McKay, K. Avalanche Breakdown in Silicon. *Phys. Rev.* **94**, 877 (1954).

117 Nishida, K., Taguchi, K. & Matsumoto, Y. InGaAsP heterostructure avalanche photodiodes with high avalanche gain. *Appl. Phys. Lett.* **35**, 251 (1979).

118 Murtaza, S. S. *et al.* Resonant-Cavity Enhanced (RCE) Separate Absorption and Multiplication (SAM) Avalanche Photodetector. *IEEE Photon. Technol. Lett.* **7**, 1486 (1995).

119 Haitz, R. H. Mechanisms Contributing to the Noise Pulse Rate of Avalanche Diodes. *J. Appl. Phys.* **36**, 3123 (1965).

120 McIntyre, R. J. McIntyre On the Avalanche Initiation Probability of Avalanche Diodes Above the Breakdown Voltage. *IEEE Trans. Electron Dev.* **20**, 637 (1973).

121 Cova, S., Ghioni, M., Lacaita, A., Samori, C. & Zappa, F. APDs and quenching circuits for single-photon detection. *Appl. Opt.* **35**, 1956 (1996).

122 Atikian, H. A. *et al.* Superconducting nanowire single photon detector on diamond. *Appl. Phys. Lett.* **104**, 122602 (2014).

123 Hayden, O., Agarwal, R. & Lieber, C. M. Nanoscale avalanche photodiodes for highly sensitive and spatially resolved photon detection. *Nat. Mater.* **5**, 352 (2006).

124 Bulgarini, G. *et al.* Avalanche amplification of a single exciton in a semiconductor nanowire. *Nature Photon.* **6**, 455 (2012).

125 Colombo, C., Spirkoska, D., Frimmer, M., Abstreiter, G. & Fontcuberta i Morral, A. Ga-assisted catalyst-free growth mechanism of GaAs nanowires by molecular beam epitaxy. *Phys. Rev. B* **77**, 155326 (2008).

126 Colombo, C., Heiβ, M., Grätzel, M. & Fontcuberta i Morral, A. Gallium arsenide p-i-n radial structures for photovoltaic applications. *Appl. Phys. Lett.* **94**, 173108 (2009).

127 Ellis, B. *et al.* Ultralow-threshold electrically pumped quantum-dot photonic-crystal nanocavity laser. *Nature Photon.* **5**, 297 (2011).

128 Sandroff, C. J., Hegde, M. S., Farrow, L. A., Chang, C. C. & Harbison, J. P. Electronic passivation of GaAs surfaces through the formation of arsenic—sulfur bonds. *Appl. Phys. Lett.* **54**, 362 (1989).

129 Bessolov, V. N., Lebedev, M. V. & Zahn, D. R. T. Raman scattering study of surface barriers in GaAs passivated in alcoholic sulfide solutions. *J. Appl. Phys.* **82**, 2640 (1997).

130 David, J. P. R., Ghin, R., Plimmer, S. A., Rees, G. J. & Grey, R. in *High Temperature Electronics, 1999. HITEN 99. The Third European Conference on* 187-190 (IEEE, Berlin, 1999).

131 Groves, C., David, J. P. R. & Rees, G. J. Temperature Dependence of Impact Ionization in GaAs. *IEEE Trans. on Electron Dev.* **50**, 2027-2031 (2003).

132 Li, Z., Gordon, R. G., Pallem, V., Li, H. & Shenai, D. V. Direct-Liquid-Injection Chemical Vapor Deposition of Nickel Nitride Films and Their Reduction to Nickel Films. *Chem. Mater.* **22**, 3060 (2010).

133 Zhang, Y. & Lončar, M. Ultra-high quality factor optical resonators based on semiconductor wires. *Opt. Express* **16**, 17400 (2008).

134 Aslam, N., Waldherr, G., Neumann, P., Jelezko, F. & Wrachtrup, J. Photo-induced ionization dynamics of the nitrogen vacancy defect in diamond investigated by single-shot charge state detection. *New J. Phys.* **15**, 013064 (2013).

135 van Oort, E., Stroomer, P. & Glasbeek, M. Low-field optically detected magnetic resonance of a coupled triplet-doublet defect pair in diamond. *Phys. Rev. B* **42**, 8605 (1990).

136 Jahnke, K. D. *et al.* Electron-phonon processes of the silicon-vacancy centre in diamond. *arXiv:1411.2871v1*.